2022-06

MODIFICATION OF COMMERCIAL ROCKET MOTORS FOR TACTICAL APPLICATIONS

Stuffle, Nathan D.

Monterey, CA; Naval Postgraduate School

NAVAL POSTGRADUATE SCHOOL

MONTEREY, CALIFORNIA

THESIS

MODIFICATION OF COMMERCIAL ROCKET MOTORS FOR TACTICAL APPLICATIONS

by

Nathan D. Stuffle

June 2022

Thesis Advisor:	Christopher M. Brophy
Second Reader:	Alexis Thoeny

THIS PAGE INTENTIONALLY LEFT BLANK

REPORT DOCUMENTATION PAGE			*Form Approved OMB No. 0704-0188*

1. AGENCY USE ONLY *(Leave blank)*	**2. REPORT DATE** June 2022	**3. REPORT TYPE AND DATES COVERED** Master's thesis

4. TITLE AND SUBTITLE MODIFICATION OF COMMERCIAL ROCKET MOTORS FOR TACTICAL APPLICATIONS	**5. FUNDING NUMBERS** R4Q04
6. AUTHOR(S) Nathan D. Stuffle	
7. PERFORMING ORGANIZATION NAME(S) AND ADDRESS(ES) Naval Postgraduate School Monterey, CA 93943-5000	**8. PERFORMING ORGANIZATION REPORT NUMBER**
9. SPONSORING / MONITORING AGENCY NAME(S) AND ADDRESS(ES) ONR/NPS	**10. SPONSORING / MONITORING AGENCY REPORT NUMBER**

11. SUPPLEMENTARY NOTES The views expressed in this thesis are those of the author and do not reflect the official policy or position of the Department of Defense or the U.S. Government.

12a. DISTRIBUTION / AVAILABILITY STATEMENT Approved for public release. Distribution is unlimited.	**12b. DISTRIBUTION CODE** A

13. ABSTRACT (maximum 200 words)

Several design modifications to commercial off-the-shelf solid rocket motors have been evaluated in support of the Naval Postgraduate School tactical rapid-response payload delivery vehicle. The modifications include a novel head-end ignition system and a tailorable nozzle end cap designed to provide reliable at-altitude ignition by improving the transient behavior of the initial combustion chamber pressure rise. The nozzle cap also provides the additional benefit of extending the shelf life of the propellant by creating an environmental seal to prevent ambient humidity from affecting the propellant. A preliminary design of a blast tube was proposed to explore how the motor exhaust could be channeled through a smaller-diameter tube before reaching the nozzle throat, thereby accommodating the volume requirements of aft fin control servos without sacrificing the overall rocket diameter or precluding use of larger-diameter rocket motors. Implementation of a blast tube also resulted in a favorable shift of the center of gravity of the rocket, which preserved and enhanced control authority during simulated fly-outs. All of the modifications were designed to be directly interchangeable with the OEM hardware to minimize the cost of implementing the new capabilities. Both the head-end ignition and nozzle enclosure systems were successfully demonstrated during flight testing, and a design process for the future implementation of a blast tube was proposed.

14. SUBJECT TERMS commercial, commercial off-the-shelf, COTS, modification, rocket, rocket motor, ignition, blast tube, forward ignition, head-end ignitor, nozzle, nozzle cap, nozzle plug, head-end ignition, tactical, tactical applications, rapid response, payload delivery, rocket propulsion, rocket propellant, commercial rocket, solid rocket motor, SRM	**15. NUMBER OF PAGES** 111
	16. PRICE CODE

17. SECURITY CLASSIFICATION OF REPORT	**18. SECURITY CLASSIFICATION OF THIS PAGE**	**19. SECURITY CLASSIFICATION OF ABSTRACT**	**20. LIMITATION OF ABSTRACT**
Unclassified	Unclassified	Unclassified	UU

NSN 7540-01-280-5500

Standard Form 298 (Rev. 2-89)
Prescribed by ANSI Std. 239-18

THIS PAGE INTENTIONALLY LEFT BLANK

Approved for public release. Distribution is unlimited.

MODIFICATION OF COMMERCIAL ROCKET MOTORS FOR TACTICAL APPLICATIONS

Nathan D. Stuffle
Lieutenant, United States Navy
BS, Embry-Riddle Aeronautical University, Prescott, 2016

Submitted in partial fulfillment of the
requirements for the degrees of

MASTER OF SCIENCE IN SPACE SYSTEMS OPERATIONS

and

MASTER OF SCIENCE IN ASTRONAUTICAL ENGINEERING

from the

NAVAL POSTGRADUATE SCHOOL
June 2022

Approved by: Christopher M. Brophy
Advisor

Alexis Thoeny
Second Reader

James H. Newman
Chair, Space Systems Academic Group

Garth V. Hobson
Chair, Department of Mechanical and Aerospace Engineering

THIS PAGE INTENTIONALLY LEFT BLANK

ABSTRACT

Several design modifications to commercial off-the-shelf solid rocket motors have been evaluated in support of the Naval Postgraduate School tactical rapid-response payload delivery vehicle. The modifications include a novel head-end ignition system and a tailorable nozzle end cap designed to provide reliable at-altitude ignition by improving the transient behavior of the initial combustion chamber pressure rise. The nozzle cap also provides the additional benefit of extending the shelf life of the propellant by creating an environmental seal to prevent ambient humidity from affecting the propellant. A preliminary design of a blast tube was proposed to explore how the motor exhaust could be channeled through a smaller-diameter tube before reaching the nozzle throat, thereby accommodating the volume requirements of aft fin control servos without sacrificing the overall rocket diameter or precluding use of larger-diameter rocket motors. Implementation of a blast tube also resulted in a favorable shift of the center of gravity of the rocket, which preserved and enhanced control authority during simulated fly-outs. All of the modifications were designed to be directly interchangeable with the OEM hardware to minimize the cost of implementing the new capabilities. Both the head-end ignition and nozzle enclosure systems were successfully demonstrated during flight testing, and a design process for the future implementation of a blast tube was proposed.

THIS PAGE INTENTIONALLY LEFT BLANK

TABLE OF CONTENTS

LIST OF FIGURES

LIST OF TABLES

THIS PAGE INTENTIONALLY LEFT BLANK

LIST OF ACRONYMS AND ABBREVIATIONS

CD	Converging-Diverging
CG	Center of Gravity
COTS	Commercial Off-The-Shelf
CP	Center of Pressure
CTI	Cesaroni Technology Inc.
FS	Factor of Safety
GNC	Guidance, Navigation, and Control
MSFC	Marshall Space Flight Center
NPS	Naval Postgraduate School
RCAF	Royal Canadian Air Force
RPL	Rocket Propulsion Lab
RPV	Rocket-Powered Vehicle
RRPD-V	Rapid-Response Payload Delivery Vehicle
SRM	Solid Rocket Motor

THIS PAGE INTENTIONALLY LEFT BLANK

ACKNOWLEDGMENTS

I would like to thank the NPS Rocket Lab staff and faculty. My deepest gratitude goes to my advisor, Dr. Brophy. Thank you for taking me on when I wandered into your lab without knowing anything about rockets. It has been a life goal of mine to complete the degree for which this thesis was written, and I owe the achievement of that goal largely to your willingness to work with me. To Alexis Thoeny, thank you for all of your assistance throughout this effort and your willingness to explain to me in copious detail why my idea(s) would not work and point me in the right direction.

Lastly, and most importantly, I want to thank my wife, Lauren. Thank you for your loving support while I subjected our family to the requirements of earning not one, but two, master's degrees at the same time. I am forever grateful for your compassion and understanding in times of stress and hardship. I love you, and I could not have done this without you.

THIS PAGE INTENTIONALLY LEFT BLANK

I. INTRODUCTION

A. BACKGROUND

Over the past two decades, technological advancements have increased the affordability of and access to microtechnology to the point where components can be commercially acquired by rogue actors and state governments alike for use in cheap instruments that can threaten American and friendly forces. The affordability and availability of such components has created a disparity between the low-cost of these technologies and the cost of countering them with expensive conventional military capabilities. A method of contending with the asymmetric cost disparity is to develop a low-cost solution to tactical problems using similar commercially available components.

One example of how microtechnology poses a threat is in an adversary's ability to cheaply constitute a drone fleet. The popularity of airborne drones has significantly increased among hobbyists and private entities thanks in part to rapid advancements in battery power and the power-to-size ratio of commercial drone motors [1]. Such advancements gave rise to the miniature form-factor of modern commercial drones and have significantly reduced the cost to consumers. With the advent of cheap, easy-to-use drone technology, commercial drones have become an alluring, easily accessible option with which extremist organizations and adversaries can threaten U.S. or friendly military and government targets.

Examples of extremist use of modern commercial drone technology include a 2013 plot by Al-Qaeda to use multiple drones against Pakistan, the incorporation of homemade and commercial-off-the-shelf (COTS) drones by the Islamic State in Iraq and Syria beginning in 2014, the 2018 assassination attempt against Venezuelan President Maduro using explosive-laden drones, and the 2018 drone swarm attacks on two Russian military bases [1]. The drones used in these examples can be easily built using COTS components or purchased fully assembled at low cost, allowing for the implementation of swarm tactics aimed at overwhelming defensive countermeasures. Figure 1 shows an example of a drone swarm.

Figure 1. Example of COTS drones swarm. Source: [1].

Countermeasures to modern drone swarms are frequently limited by cost due to the number of countermeasures required and their ability to autonomously engage multiple targets simultaneously. Electronic attack can be a cost-effective solution to disabling small numbers of unprotected COTS drones, but purely electronic means of defense become more complicated as swarm numbers increase or if the drone operators implement electronic counter-countermeasures through electronic hardening and enhanced cybersecurity software [2]. Therefore, an optimal strategy for engaging adversary drones should include some form of autonomous kinetic kill capability. Modern self-guided missiles possess enough capability to engage swarms at long distances and accurately target incoming drones [2], however, the costs of using such systems is prohibitively high. Even small semi-active seeker missiles, such as the Hellfire, exceed $100,000 per unit [3]. When compared to the low cost of reconstituting a COTS drone fleet, it becomes obvious that the asymmetric cost of deploying current military missile systems to achieve autonomous kinetic kills against drone swarms is unsustainable.

In 2016, the Naval Postgraduate School (NPS) Rocket Propulsion Laboratory (RPL) initiated development of a low-cost autonomous kinetic kill response to the small drone threat. This project features a rocket-powered vehicle (RPV) built from the ground up by RPL students and staff using COTS solid rocket motors (SRM) and commercially available guidance systems and avionics. An early model of the RPV is depicted in Figure

2. Early iterations of the project focused on the aerodynamics, structure design, booster separation, and guidance, navigation, and control (GNC) needed to maneuver the vehicle to the target location. Such work was initiated by ENS Fletcher Rydalch, USN in 2016 and refined by CAPT Kai Grohe, Royal Canadian Air Force (RCAF) the following year.

Follow-on work began to focus on the design of bomblet submunitions that are intended to be deployed from the RPV sled following apogee booster separation. CAPT Keith Lobo, RCAF designed the bomblet depicted in Figure 3. The submunitions are designed to fall under the control of maneuverable air brake fins and terminally self-guide into the target using onboard sensors.

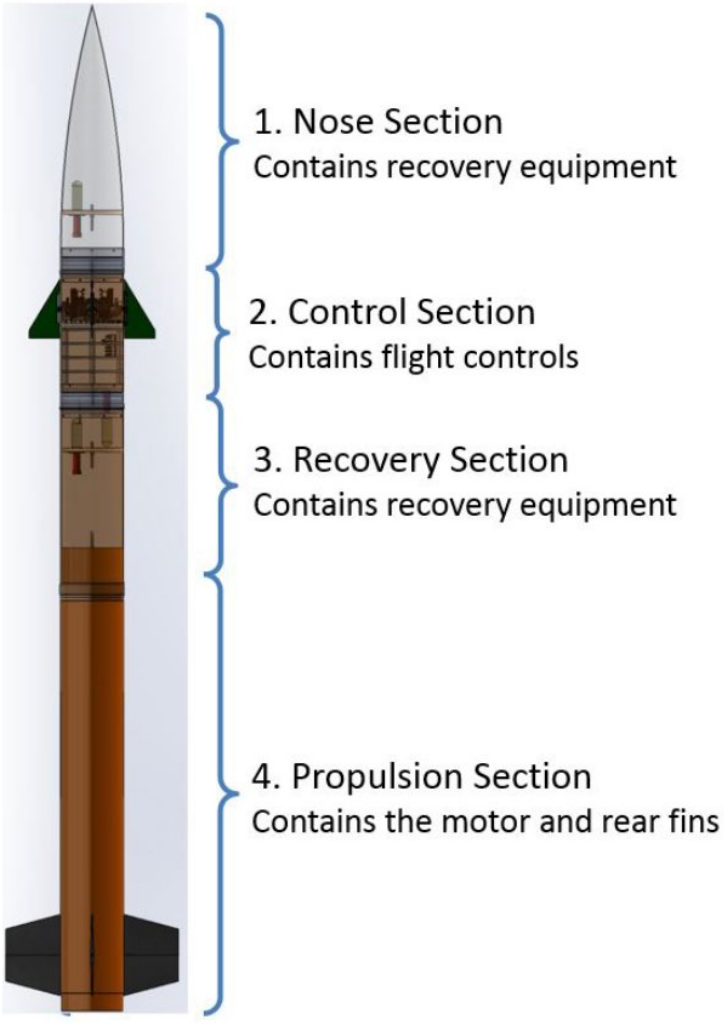

Figure 2. 2017 model of NPS RPV. Source: [4].

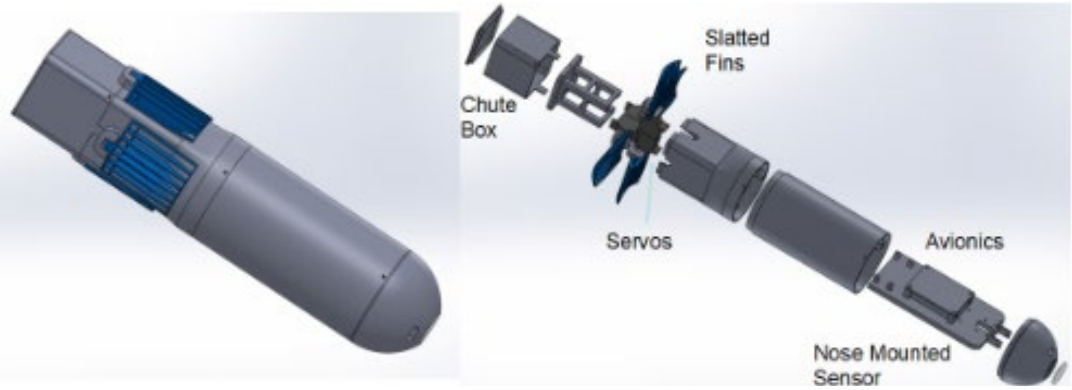

Figure 3. 3D bomblet model. Source: [5].

Figure 4 visually depicts the concept of employment for the RPV. The intent is to provide a fire-and-forget quick-launch response capability on a single-stage solid rocket booster given a general location. The RPV will maneuver to a given latitude, longitude, and altitude. Following booster separation at apogee, the vehicle sled will fall towards Earth under a drogue parachute or other aerobraking mechanism. Once sensors in the nose cone detect drones, the bomblet will be released to intercept the targets.

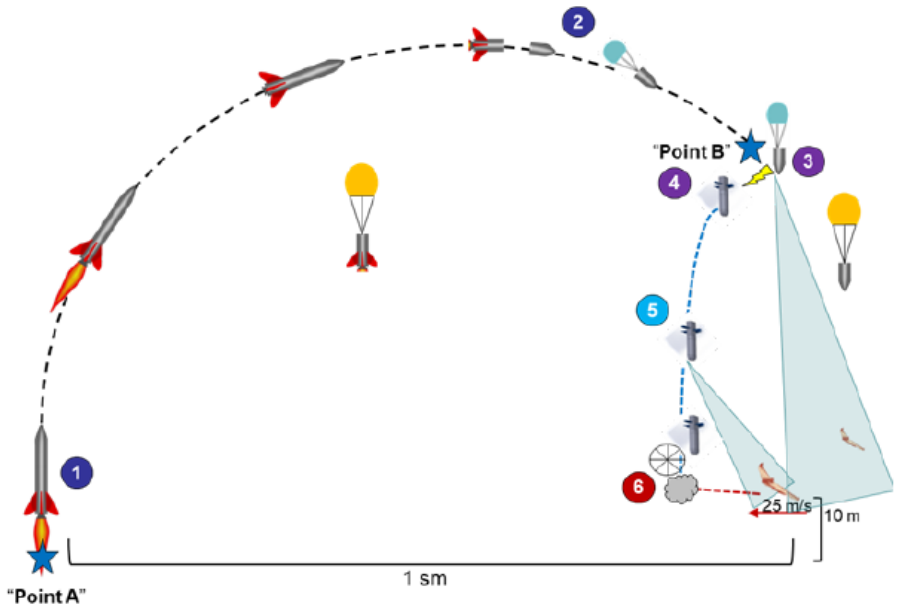

Figure 4. NPS anti-drone bomblet concept of employment. Source: [6].

More recent iterations of the RPV focused on including multiple deployable bomblets as well as a possible second stage rocket motor. Figures 5 and 6 show the overall multi-bomblet RPV and 3D model for a deploying mechanism, respectively, as designed by LT Matthew Busta, USN, and LT Robert Thyberg, USN, in 2019 [7].

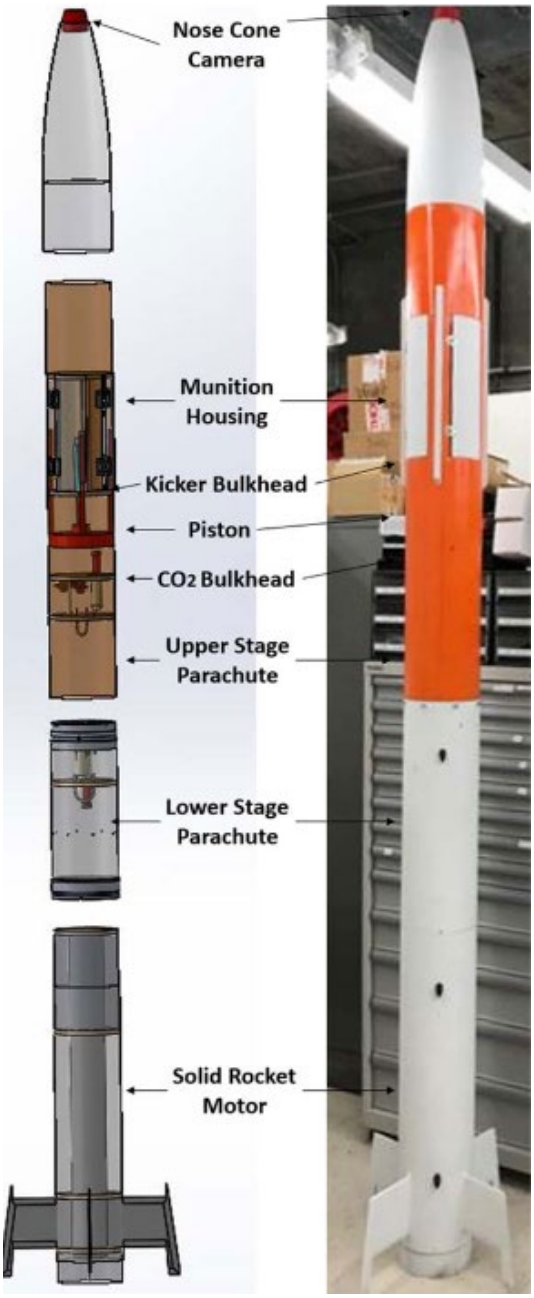

Figure 5. 2019 RPV multiple bomblets design. Source: [7].

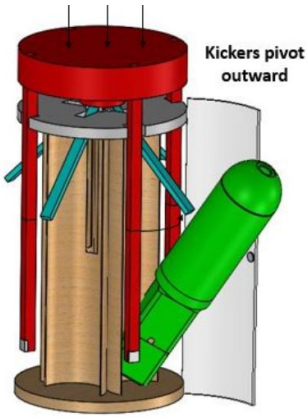

Figure 6. Multi-bomblet deploying mechanism. Source: [7].

The current direction of the project seeks to expand the application of the RPV to include acting as a rapid-response payload delivery vehicle (RRPD-V) that can be adapted for various mission sets, as outlined in Figure 7. Mission "A" of Figure 7 depicts the deployment of a high-altitude communications relay that provides a rapidly deployable over-the-horizon communications capability. Mission "B" depicts a use concept similar to the bomblet concept of deployment shown in Figure 4. In this case, however, the bomblet bay can be changed out for any payload of appropriate size, allowing for low-cost rapid delivery, including in denied areas.

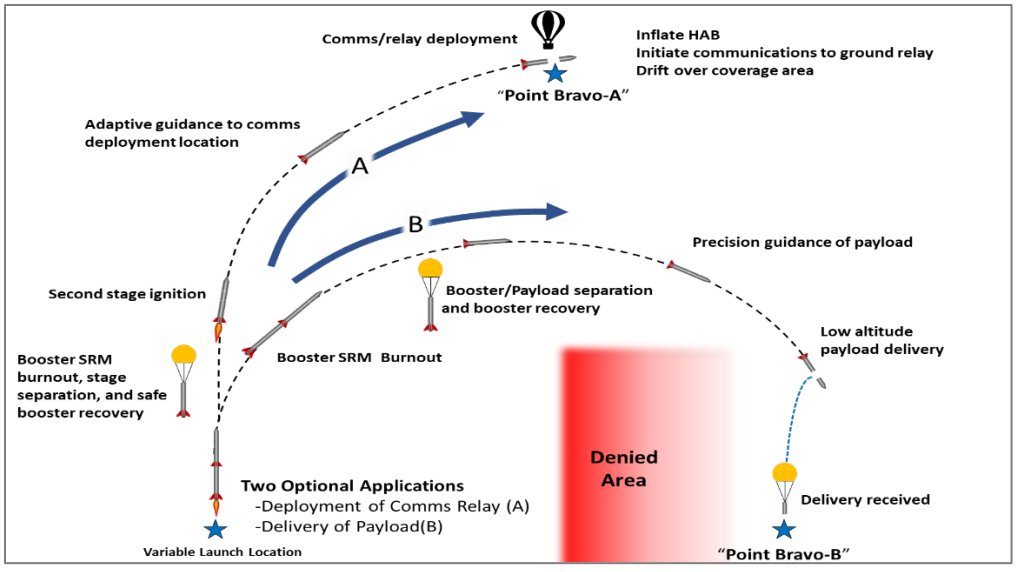

Figure 7. NPS RRPD-V multi-mission concept. Source: [8].

The requirements for the eventual use of these system design options are to provide a system that is steerable, that can be fired on-demand, and has a minimal manufacturing cost to keep the threat response cost symmetric.

B. MOTIVATION

The NPS RPL has made several attempts at developing a two-stage solid propellant rocket. Two attempts in 2018 resulted in mid-air breakups of the RPV at the point where staging was expected to occur. Although the suspected cause for these breakups was failure of the interstage coupler, the exact reasons were indeterminate [4]. In both cases, the second stage SRM failed to ignite.

More recently, a 2020 attempt of a two-stage launch failed less than three seconds into flight as the bending torque created by the addition of weight in the nosecone to manipulate the rocket's center of gravity (CG) proved too high for the booster-to-interstage mating coupler [6]. Figure 8 shows the moment of failure as captured by video from the ground. Although improvements to the structural integrity of the system are being addressed, the desire for reliable ignition of the second stage remains.

Figure 8. Fall 2020 two-stage mid-flight failure. Source: [6].

The inclusion of a second stage will add versatility to the RRPD-V in terms of range and altitude capabilities. Single-stage systems are limited in motor size, and therefore range, by the diameter of the rocket body. Larger diameter booster SRMs can preclude the use of aft fin control servos due to space limitations and can complicate GNC by shifting the vehicle CG aft of the center of pressure (CP), possibly creating an unstable control condition during motor burn and the subsequent fly-out. Additionally, propellant mass depletion during flight will cause the CG to shift, introducing potential challenges for the system guidance and control due to the shift of the CG. Figure 9 illustrates how having a CG forward of the CP creates a stable condition.

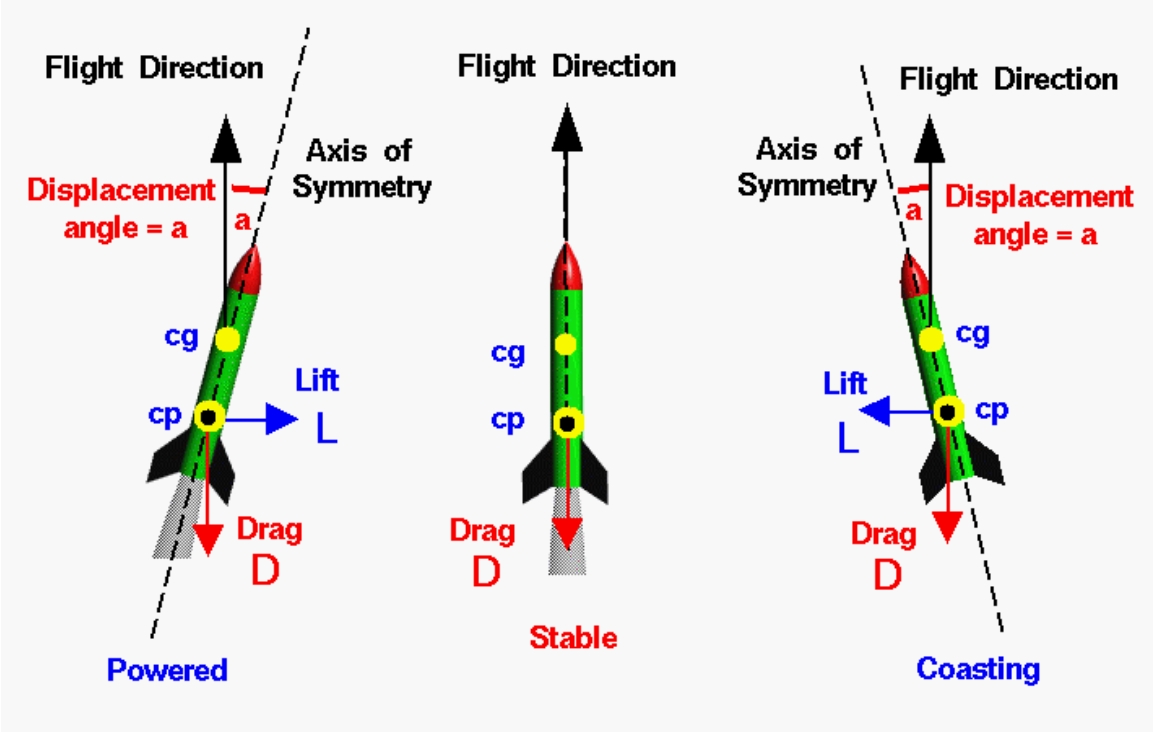

Figure 9. NASA rocket stability demonstration. Source: [9].

One of the complications of introducing a second-stage motor, however, is inclusion of a reliable mechanism with which to ignite the second motor. In the world of amateur rocketry, it is common practice to ignite commercial SRMs via a pyrotechnic squib attached to a semi-flexible lead that is fed through the nozzle, up the aft end of the rocket.

The vibration and acceleration loads during boost make a similar aft-end ignition approach unreliable for the second stage, as the squib may become dislodged and misaligned. Furthermore, any excess material, such as a semi-flexible lead, can act as a liability, potentially clogging the nozzle throat as the material is expelled. Even a partial throat clog for a short duration can cause a jump in motor chamber pressure that could rupture the motor case. For the purpose of the RRPD-V, the second stage ignition system must also be reliable, easily implemented, and directly controlled by the onboard avionics electronics.

Implementation of a head-end ignition system will improve the structural integrity and effectiveness of the ignition squib and also allow for the inclusion of an aft nozzle enclosure. The nozzle enclosure will hermetically seal the propellant within the motor chamber during storage. Solid rocket propellants deteriorate over time due to environmental storage factors, especially from the absorption of water due to humidity. This deterioration occurs at a faster rate than that of other rocket systems, causing the shelf life of the rocket to be determined by the longevity of the propellant [10]. A hermetically sealed chamber will help reduce inconsistency in propellant behavior born from differences in storage environments and increase the reliability and repeatability among motors that have been stored for various amounts of time.

A second improvement gained from implementing a nozzle seal is to promote a rapid ignition sequence by designing the sealing enclosure such that it allows for a rapid buildup of pressure and yields once a predetermined chamber pressure is reached. COTS SRMs typically exhibit longer ignition transient times, between when the ignition is triggered and when maximum thrust is achieved, than do tactical military SRMs, which always include such enclosures. Figure 10 shows the representative thrust curve, as provided by the manufacturer, of the Cesaroni M1540 75mm five-grain SRM used for this work.

The curve exhibits an underdamped time response to ignition before following a regressive burn pattern until the propellant is exhausted. For this specific propellant mixture, the peak thrust is not reached until approximately 0.33 seconds post-ignition without including any delay between the ignition squib firing and the initial buildup of pressure. This is the point at which the maximum available propellant surface area is

burning for a regressive burn propellant geometry. Prior to this peak, the motor will eject propellant mass at off-design chamber conditions. A nozzle seal enclosure helps minimize the escape of mass from the chamber during the ignition transient with the goal of producing a rapid and reliable ignition event with a thrust curve that more closely resembles a Heaviside step function.

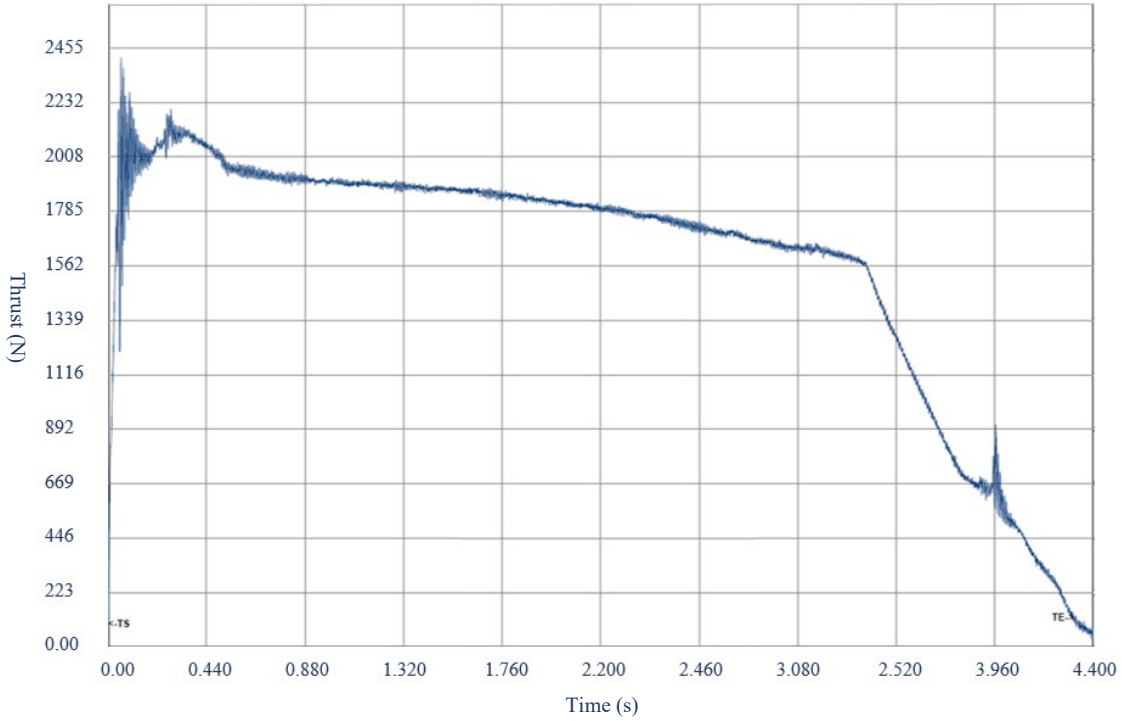

Figure 10. Cesaroni M1540 representative thrust curve. Adapted from [11].

Finally, the inclusion of a blast tube will allow for the use of larger diameter motors that can maximize volumetric efficiency while maintaining a minimum-diameter rocket body. In an aft fin-control guided booster stage, the SRM must contend for radial space with the fin control servos. A blast tube would function as an extension of the motor chamber prior to the nozzle throat with a reduced diameter that will allow the flow of a large-diameter SRM to be directed to the nozzle through a diameter that allows for the volume requirements of fin control servos around the blast tube.

A secondary effect of a blast tube is that it can favorably shift the CG of the motor, and therefore the RPV, forward. Because of the significant mass of the SRM with respect to the rest of the rocket components, its placement has a large impact on the location of the overall vehicle CG. If the CG is too far aft, the rocket will be unstable. Figures 11 and 12 depict the location of the CG and CP of a hypothetical single-stage RPV with and without a blast tube.

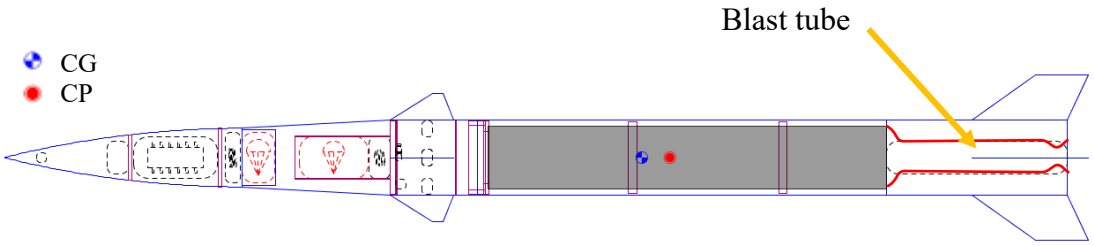

Figure 11. Hypothetical rocket model with a blast tube (stable). Adapted from [12].

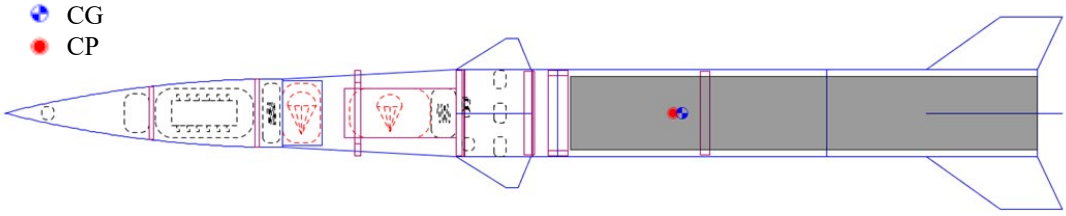

Figure 12. Hypothetical rocket model without a blast tube (unstable). Adapted from [12].

C. OBJECTIVES

This study aims to support the NPS RPL rapid-response payload delivery vehicle by providing low-cost modifications to COTS rocket components to enhance their performance and applicability for tactical missions. To that end, the objectives of this effort include:

- Design and implement a head-end ignition system for use in a multi-stage rocket that utilizes COTS solid rocket motors.
- Design and implement an aft nozzle enclosure along with an in-flight rocket motor chamber pressure monitoring system.
- Propose a design geometry and material for a blast tube for future manufacture and integration between the COTS solid rocket motor and nozzle.

II. APPROACH

A. HEAD-END IGNITION SYSTEM

The design and integration of an autonomous head-end ignition system for the RPV second stage motor leveraged as much of the vendor-provided hardware as possible. Experimental ground tests guided the design such that the system could reliably ignite a solid propellant motor, and follow-on flight tests demonstrated the system's ability to operate effectively under flight conditions. 3D printing was identified as the preferred method of manufacture of consumable components, as it allowed low-cost, quick prototyping with resources that were available within NPS and specifically at the Rocket Propulsion Lab. Criteria for material selection included strength, melting temperature, ductility, and ease of printing. The squib holder geometry was selected based on ease of integration into existing COTS hardware and performance characteristics of two primary holder categories. These categories included a directed-flow squib housing and an open, unrestricted holder. The ignition squib holders were subjected to laboratory testing and evaluation, in which high-speed video recording was used to analyze a series of ignition sequence characteristics. These characteristics included size, duration, and direction of the flow of ejected hot material. The laboratory tests also ensured that the system was capable of being triggered with electronic hardware that was onboard the rocket. A squib holder design was then chosen for use in a static ground live-fire test of a commercial SRM and was later integrated into the RPV second stage for in-flight testing of the autonomous sustainer ignition capability.

B. NOZZLE ENCLOSURE SYSTEM

All tactical missile systems have some way of isolating the propellant in an SRM from ambient conditions. The enclosure designs often involve a plug or a cap placed in or around the nozzle to create a hermetic seal. This enclosure device was designed to be ejected once a predetermined chamber pressure was reached.

The designs that were considered were developed using 3D modeling software based on the geometry of the COTS rocket nozzles and then 3D printed. These prototypes

underwent a series of laboratory pressure tests, static motor live-fire tests, and rocket flight tests. The selection of the final design that was integrated into the RPV was based on repeatability of the blowout conditions, as determined by the laboratory pressure tests, and performance measurements taken during the static motor live-fire tests.

The blowout condition was determined based on the pressure created by the squib ignition process. The data was obtained by initiating an ignition squib within an enclosed space representative of the open volume within the motor chamber. This volume was monitored by a pressure transducer that measured the increase in pressure that could be expected within a sealed motor. The blowout condition was then set at some margin above this pressure to avoid premature enclosure ejection.

The seal was made via O-ring contact with the nozzle. This study investigated methods of contact to include a plug that contacted the internal surface of the nozzle and an exterior cap that sealed around the outer surface of the nozzle. High-speed video recording and a chamber pressure monitoring system were used during static live-fire tests to analyze and compare the ability of each design to maintain a seal against gas leaks during the ignition process.

Several methods of securing the nozzle enclosure to the rocket were also investigated. This portion of the enclosure system was designed to yield at a desired force due to the applied pressure. The application of nylon shear pins as well as 3D printed leverage arms were tested. Determination of the preferred securing method was made based on the ability of each method to prevent leakage and the repeatability of achieving the desired yield point. Repeatability testing was conducted in a laboratory setting by regulating the pressure in a controlled space. High-speed video recording and pressure monitoring observed the securing mechanism's ability to prevent leaks during static live-fire tests.

C. BLAST TUBE

A blast tube design was investigated in order to demonstrate the proof of concept for incorporating a custom-designed blast tube into a commercial rocket motor and identify a material with which it may be manufactured in the future. Industry standards were

researched and leveraged in order to design a geometry and provide a recommended manufacturing method.

THIS PAGE INTENTIONALLY LEFT BLANK

III. DESIGN PROCESSES

A. HEAD-END IGNITION SYSTEM

The design for the head-end ignition system was born of the need for a reliable, autonomous second-stage ignitor and the simultaneous requirement to seal the aft end of the SRM. Two main requirements were identified at the outset of the design process—the ignitor squib needed to remain secure during the booster phase of flight, and the system needed to reliably light the solid propellant. A Cesaroni Technology Inc. (CTI) commercial squib was secured to 2 g of ammonium perchlorate-based solid propellant, as shown in Figure 13. The head-end ignition system and accompanying electronic hardware needed to be able to deliver the required voltage and current to the squib and also be compatible with the existing forward retaining hardware, imaged in Figures 14 and 15. Figure 16 shows how the wire leads feed through the forward hardware.

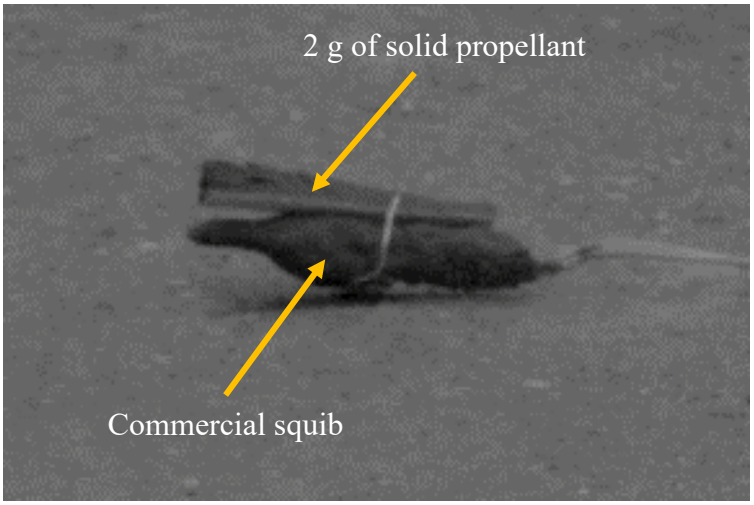

Figure 13. Ignition squib with 2 g of solid propellant attached

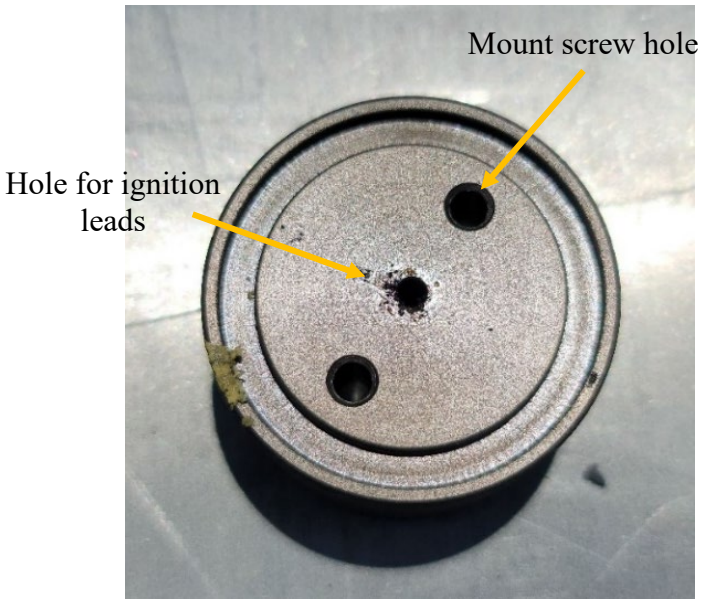

Figure 14. Smoke charge replacement hardware

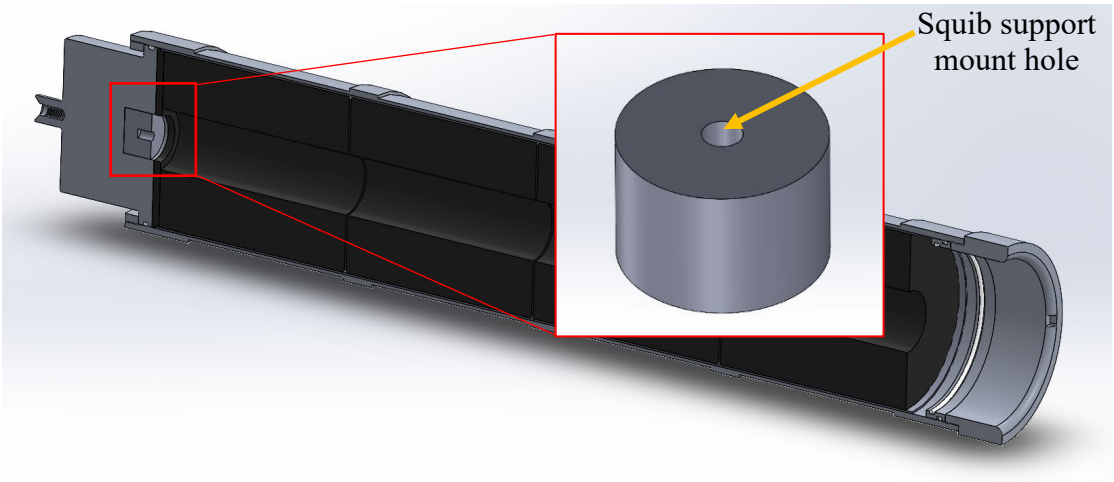

Figure 15. Smoke charge replacement hardware within 4-grain SRM 3D model cutaway

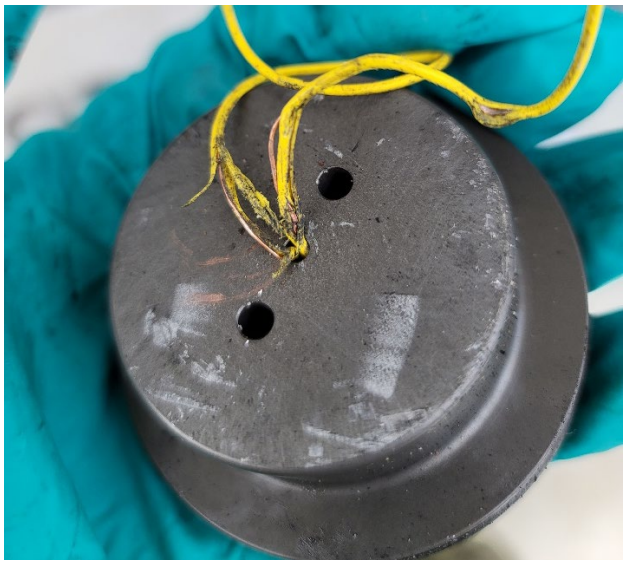

Figure 16. Head-end ignition leads post-fire

Commercially available JBKwik epoxy was used to bond the holder and wires to create a pressure seal between the wire leads and the forward retaining hardware. The epoxy was selected for its 15-minute set time, which was ideal for quick launch site assembly.

1. Ignition Squib Holder Version 1

Early iterations of the system focused on a 3D printed perforated basket that was designed to hold the squib. The perforations consisted of holes meant to create hot jets from the squib material that would be directed at and ignite the propellant. Polycarbonate was selected as the printing material for its high melting temperature (300°C [13]) vs. that of PLA (151°C [14]). The intent behind this selection was to ensure the integrity of the basket throughout the ignition and combustion process. Several variations on basket size and hole placement were investigated. An example of this design is given in Figure 17.

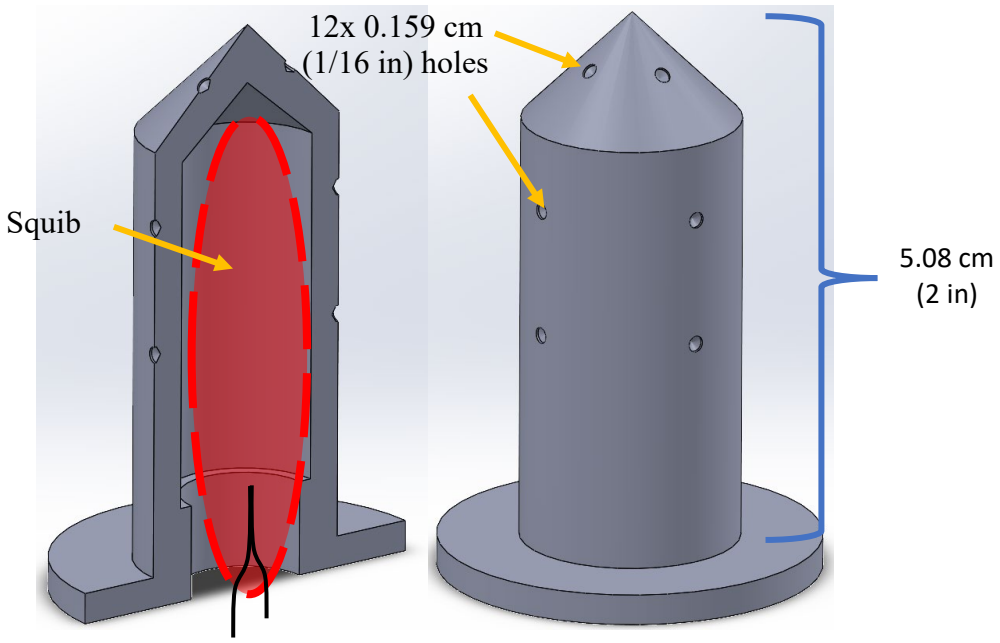

Figure 17. Squib basket 3D model hole configuration C1

After the design was printed, the holes were drilled out with a 0.159 cm (1/16 in) drill bit. The basket variation depicted in Figure 17 featured eight radial holes—four sets of two vertically-aligned holes separated by 90°. Four additional holes were positioned on the tip of the basket in azimuthal alignment with the pairs. The basket tip was angled at 45° from vertical in order to give the hot jets an axial vector component. Placement of the holes intentionally began 1.91 cm (3/4 in) above the base of the basket to ensure the jets made contact with the propellant without striking the motor forward retaining hardware directly. The two other hole configurations that were tested are shown in Figure 18.

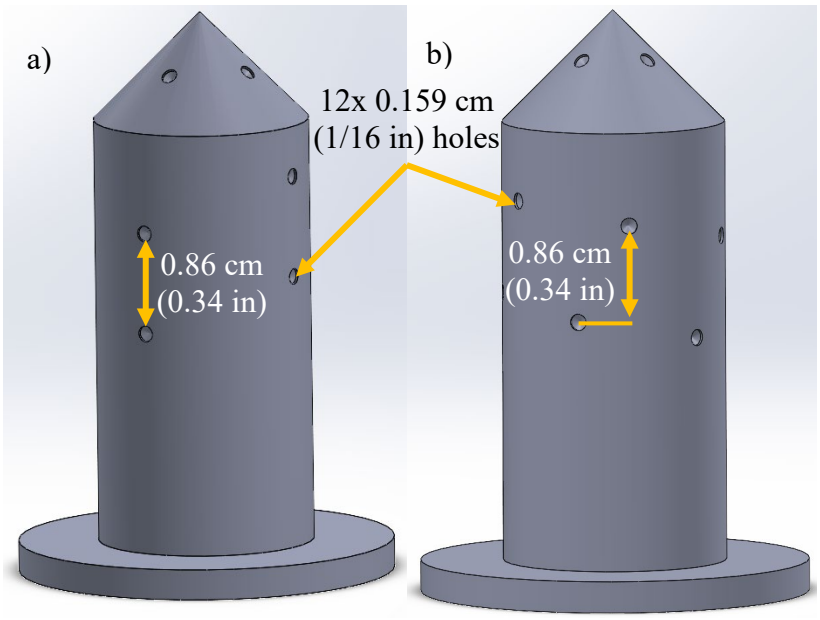

Figure 18. a) Hole configuration C2. b) Hole configuration C3

Hole configurations C2 and C3 incorporated axial and azimuthal offsets, respectively, between the holes in an attempt to achieve greater propellant surface area coverage by the jets. Configurations C2 and C3 each had 12 holes.

A 7.62 cm (3 in) long version of the basket was also tested with the same hole configurations. The extra length of this version allowed both for a larger squib and for a third row of holes as shown in Figure 19. Each configuration was tested with a squib-propellant combination as imaged in Figure 13. With the squib inserted into the basket, the ignition lead wires were fed through the forward retaining hardware assembly and secured with JBKwik epoxy cold weld. Figure 20 shows a profile view of the test article assembly secured in the test stand.

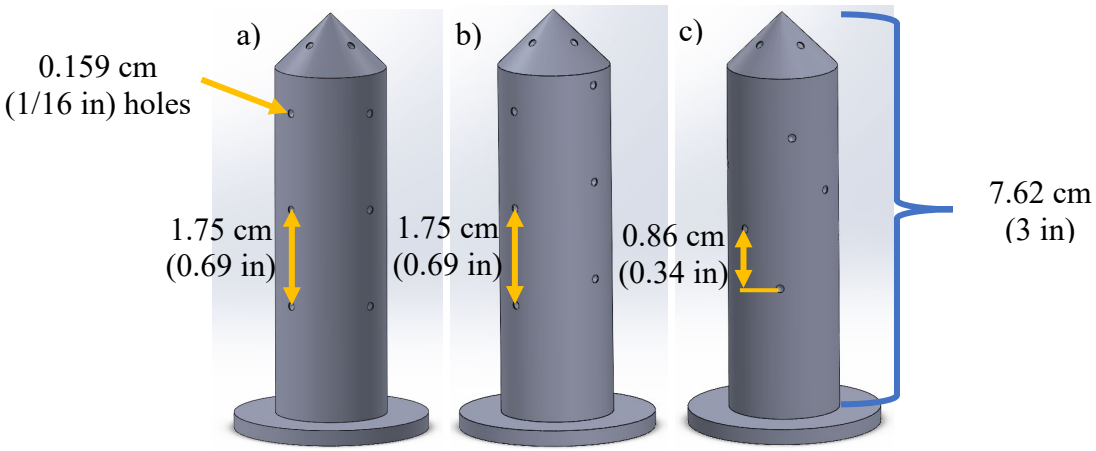

Figure 19. 7.62 cm (3 in) basket in configurations a) C1, b) C2, and c) C3

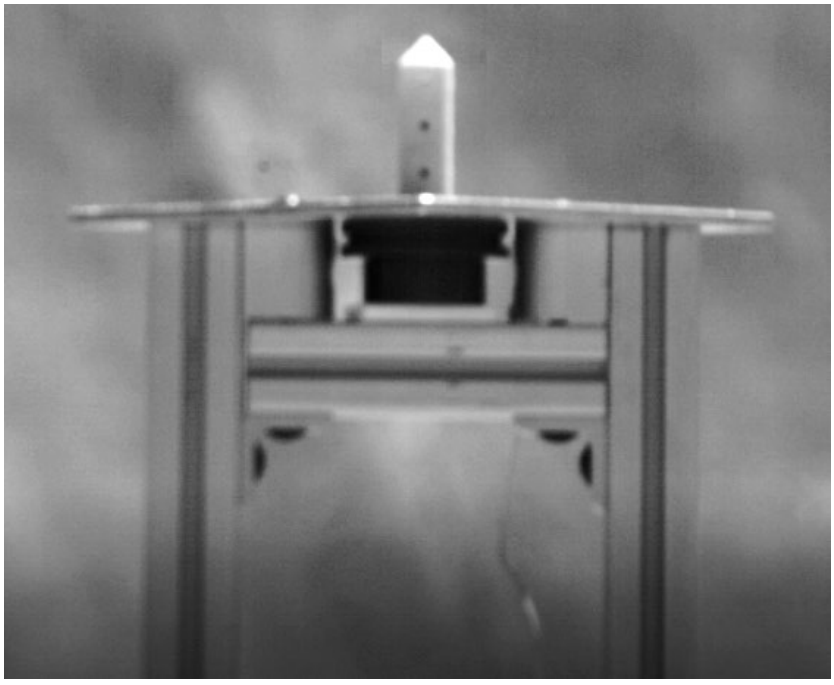

Figure 20. Test stand setup with 7.62 cm (3 in) C1 basket

Figure 21. High-speed camera and test stand setup

High speed video of the ignition process was recorded at a rate of 10,000 frames per second. These videos were used to evaluate the performance of each basket based on jet development reponse time, jet fullness, and jet duration. The video brightness was reduced to better visualize the hot gas jets. Figure 22 shows a still image of the jets produced by a 7.62 cm (3 in) basket with 0.159 cm (1/16 in) holes. The gas jets extruding from the basket tip were clearly visible, while the radial holes remained mostly dark. Visual inspection of the basket post-firing revealed that the ignition of the squib created slag that clogged many of the holes, preventing the gas from escaping, as can be seen in Figure 23.

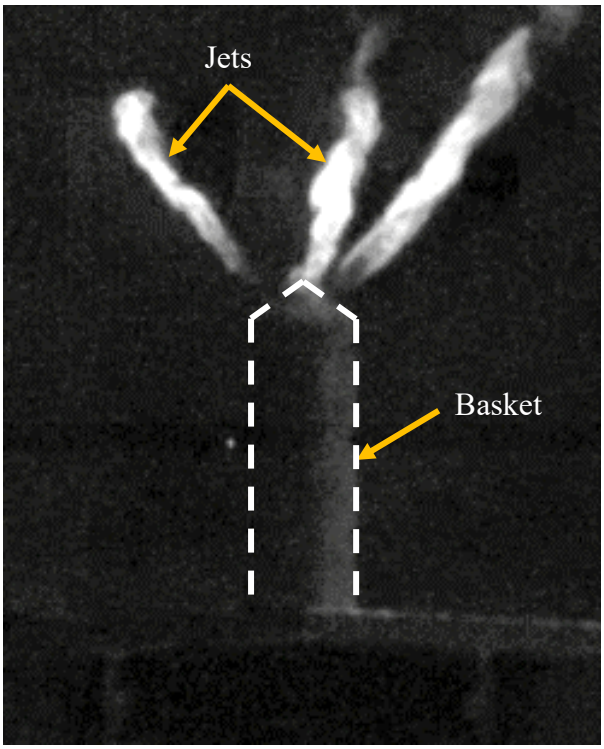

Figure 22. 7.62 cm (3 in) basket with 0.159 cm (1/16) in holes high-speed camera still frame

Figure 23. Post-fire 7.62 cm (3 in) basket with clogged holes

To remedy the clogging issue, the hole diameters were enlarged for subsequent tests. A combination of 0.238 cm (3/32 in) and 0.318 cm (1/8 in) holes were used for the test of the 5.08 cm (2 in) basket shown in Figure 24a. The bottom row of holes was drilled out to a 0.318 cm (1/8 in) diameter, while the rest were drilled out to 0.238 cm (3/32 in). Figure 24b highlights the contrast between the hole sizes. While neither size resulted in clogging, the larger holes allowed for a significant increase in mass flow and a corresponding increase in the size of the jets.

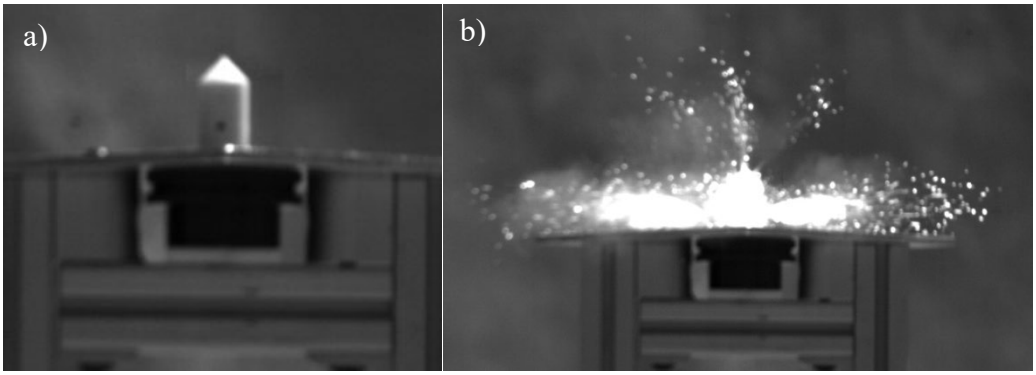

Figure 24. 5.08 cm (2 in) basket with combination hole sizes a) before and b) during ignition

2. Ignition Squib Holder Version 2

Because of the length of the first version of the basket, concerns existed over a potential nozzle throat clog in the event the basket became dislodged during the motor burn. The relationship between chamber pressure P_c and the nozzle throat area A_{th} for steady-state operation of a solid rocket motor is given by Equation 1.

$$P_c = \left[\frac{A_b a \rho_p C^*}{A_{th} g_c} \right]^{\frac{1}{(1-n)}} \tag{1}$$

The burn rate constant a, the propellant density ρ_p, the characteristic exhaust velocity C^*, and the gravitational constant g_c, can be considered constant for a given

propellant. The propellant burn area A_b is also close to constant for a neutral burn profile. Therefore, it follows that

$$P_c \propto \left[\frac{1}{A_{th}}\right]^{\frac{1}{(1-n)}} \tag{2}$$

where n is the burn rate exponent specific to the propellant chemical makeup and is a value less than 1. Typical n values for a high burn rate solid propellant grain are given in Table 1.

Table 1. n values at various pressure ranges. Adapted from [15].

Pressure Range (MPa)	n-Variation
6.865-11.77	0.35-0.36
11.77-14.71	0.44-0.45
14.71-19.61	0.47-0.48
19.61-22.56	0.58-0.59

The relationship in Equation 2 reveals that as A_{th} is reduced, the pressure within the chamber increases substantially. According to Equation 2, an SRM with a propellant burn rate exponent of 0.4 that has its nozzle throat area reduced by half will experience a 317% increase in chamber pressure. Assuming a standard factor of safety (FS) for expendable launch vehicles of 1.4 [16], the motor case would certainly rupture. Even a small blockage that results in a pressure build below the FS margin could still result in undesirable nozzle flow which could lead to flow separation from the nozzle walls. This could cause unpredictable thrust vectoring and loss of control.

It was therefore imperative that the head-end ignition system be redesigned such that the dislocation of part or all of the squib holder during motor burn would not result in nozzle throat blockage. This limited the size of the ignition basket to less than the diameter of the nozzle throat, measured as 2.45 cm (0.966 in). This axial length constraint eliminated

the possibility of including radial jet holes. Two different methods for compensating for the reduction in the number of holes were tested. The first approach was to increase the size of the hole diameters to the maximum that space would allow, which was 0.476 cm (3/16 in). Four holes of this size created a total hole surface area of 0.710 cm^2 (0.110 in^2) or 150% of the hole surface area of the ignition basket shown in Figure 19. The second approach incorporated four additional holes, making a total of eight, each drilled out to a 0.318 cm (1/8 in) diameter. The resulting total surface area was 0.632 cm^2 (0.098 in^2). Figure 25 depicts a 3D model of the new ignition basket variant with the eight-hole arrangement.

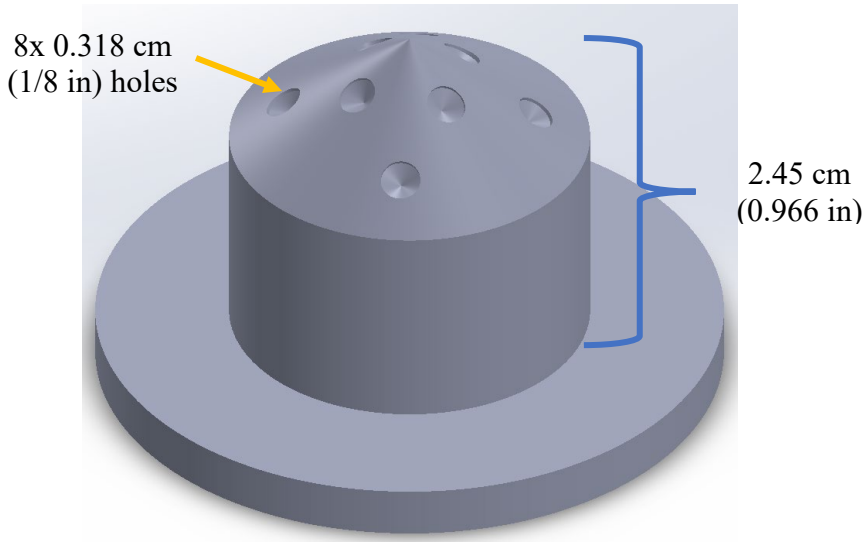

Figure 25. Ignition basket version 2 with 8 holes

Each of the new ignition basket variants were tested in the same manner as the version 1 variants. High-speed video capture was used to compare the performance of the hot gas jets. Figures 26 and 27 show the comparable size and thickness of the jets as well as the hot particulate that the squib expelled.

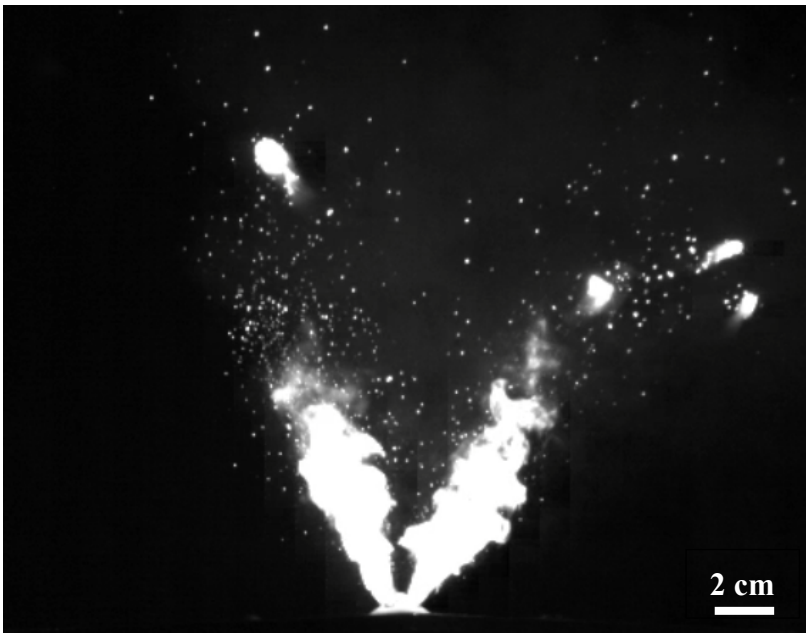

Figure 26. Ignition basket version 2 with 0.476 cm (3/16 in) holes test high-speed camera still frame

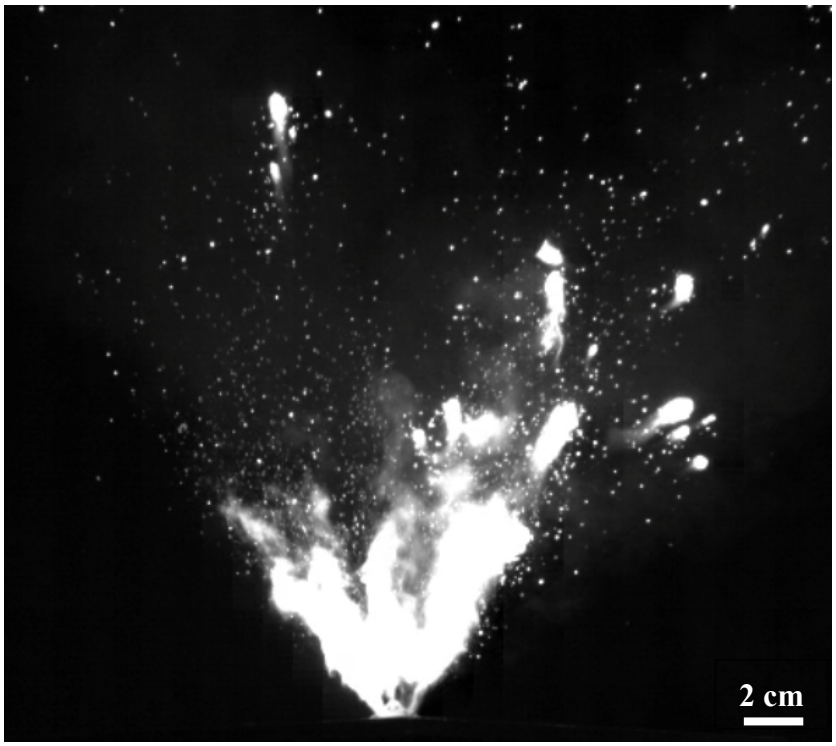

Figure 27. Ignition basket version 2 with 0.318 cm (1/8 in) holes test high-speed camera still frame

While the images showed that the ignition basket with 0.476 cm (3/16 in) holes created wider jets, the length and duration of the jets did not change appreciably between the two tests. The most notable difference between the two variants was the spread of the expelled material. The 0.318 cm (1/8 in) hole variant created a much more evenly dispersed cone of hot gas and particulate, offering the advantage of striking a larger portion of the propellant grain surface area. The 0.318 cm (1/8 in) hole variant was chosen for static live-fire testing for this reason. Because of the reduced ignition basket size, however, a smaller squib had to be used. In static SRM tests, the smaller squib failed to expel enough energetic material to light the propellant. A second squib needed to be inserted through the nozzle in order to ignite the motor. Figure 28 shows the SRM in the test stand.

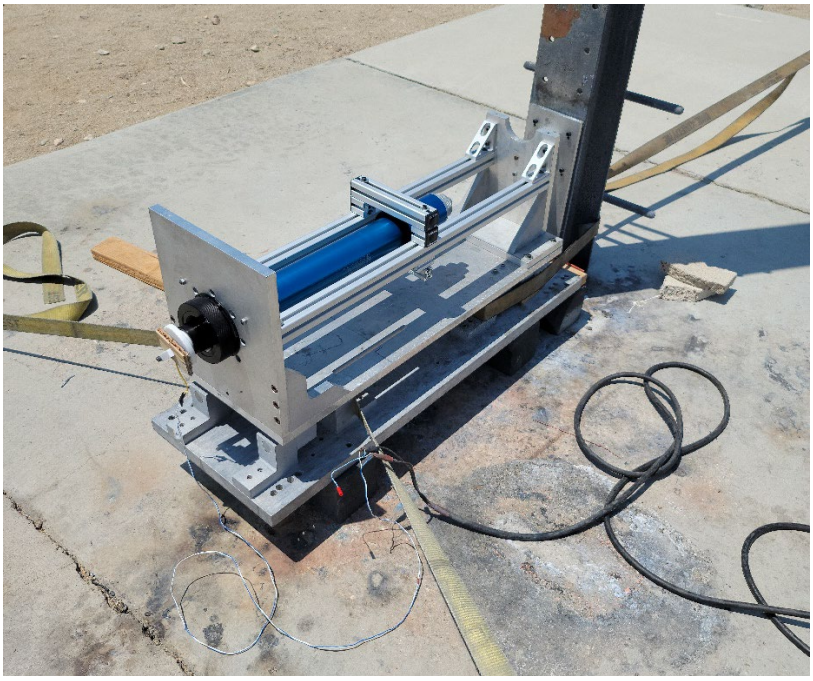

Figure 28. Static SRM live-fire test stand setup

Post-fire visual inspection of the test stand and motor revealed another critical failure in the current design; the ignition system failed to prevent a leak through the head-end hardware. Figures 29 and 30 show the clearly visible scorch marks left by the leak. Such a leak during flight would likely destroy the flight electronics that reside forward of

the motor and cause a catastrophic failure. The cause of the leak was determined to be an imperfect seal in the port of the forward retaining hardware, shown in Figure 30, through which the wire leads were fed. These test results led to the design of version 3 of the ignition system.

Figure 29. Test stand head-end after live-fire test

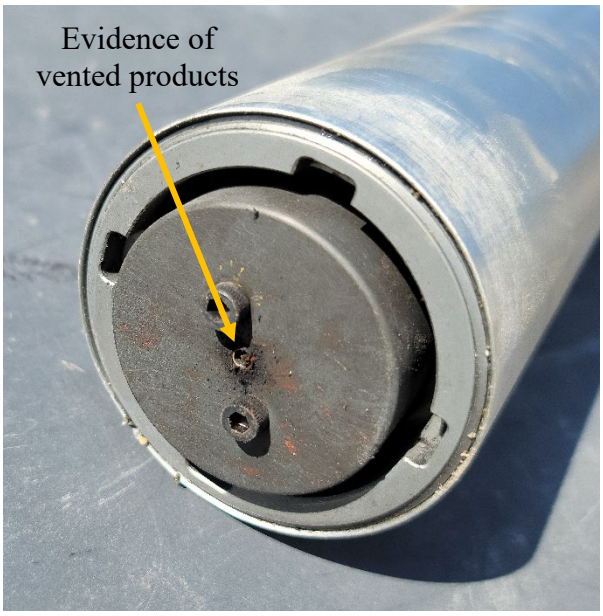

Figure 30. Exterior of motor head-end retaining hardware after live-fire test

3. Ignition Squib Holder Version 3

The design for version 3 of the ignition squib housing focused on allowing the use of a larger amount of energetic material without introducing the risk of throat blockage. Critically, the design also needed to assure against leakage through the forward retaining hardware. To meet these requirements, the design approach was changed to an open holder that secured the squib in place with semi-flexible supports, shown in Figure 32, rather than a perforated basket. This approach prevented the limitations that the basket housing imposed on the size of the squib. To accommodate the size of squib pictured in Figure 13, however, the holder length needed to be longer than the 2.45 cm (0.9660 in) diameter of the nozzle throat. To reduce the risk of throat blockage, the supports needed to be designed to melt in the extreme temperature of the motor chamber. Figure 31 shows that most of the polycarbonate basket remained intact but had started to melt away from the base, demonstrating the threat of nozzle clogging from large debris posed by this design. It was therefore necessary to change the material with which the housing was printed. PLA, which has a melting temperature of about half that of polycarbonate [13, 14], was selected for this purpose.

Figure 31. Ignition basket version 2 after live-fire test

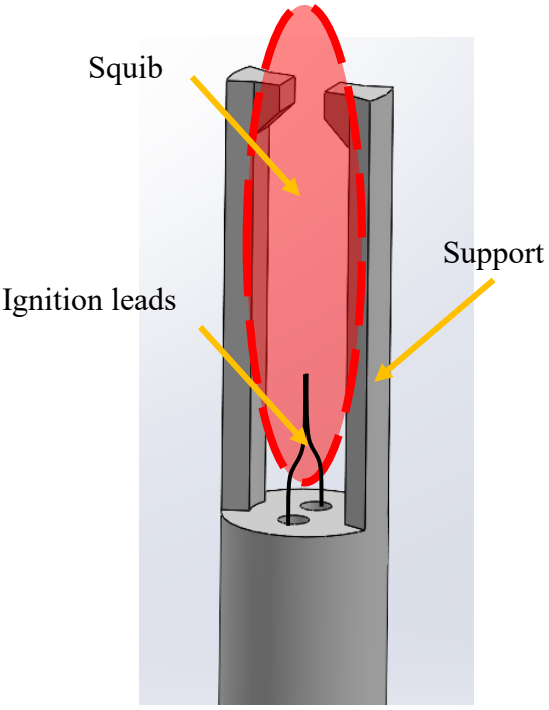

Figure 32. Semi-flexible squib holder supports

The final design consideration focused on how the squib holder seated into the COTS forward hardware and prevent the escape of gas through the head end. Rather than rely on the epoxy seal between the wire leads and the forward hardware alone, the new design fit into the smoke charge replacement puck and the wire leads were split before

being threaded through the holder and individually sealed with epoxy. Figure 33 shows a 3D model cutaway of the squib holder seated in the smoke chare replacement puck.

JBKwik was again selected as the bonding agent for the wire leads. A modified version of the holder, shown in Figure 34, was printed for laboratory pressure testing. The wire leads were coated in JBKwik and individually threaded through the holes in the test article. Additional JBKwik was added to where the wires exited the article to ensure that no gaps existed. Laboratory tests at room temperature demonstrated that JBKwik was able to withstand at least 5.17 MPa (750 psi) without any leaks.

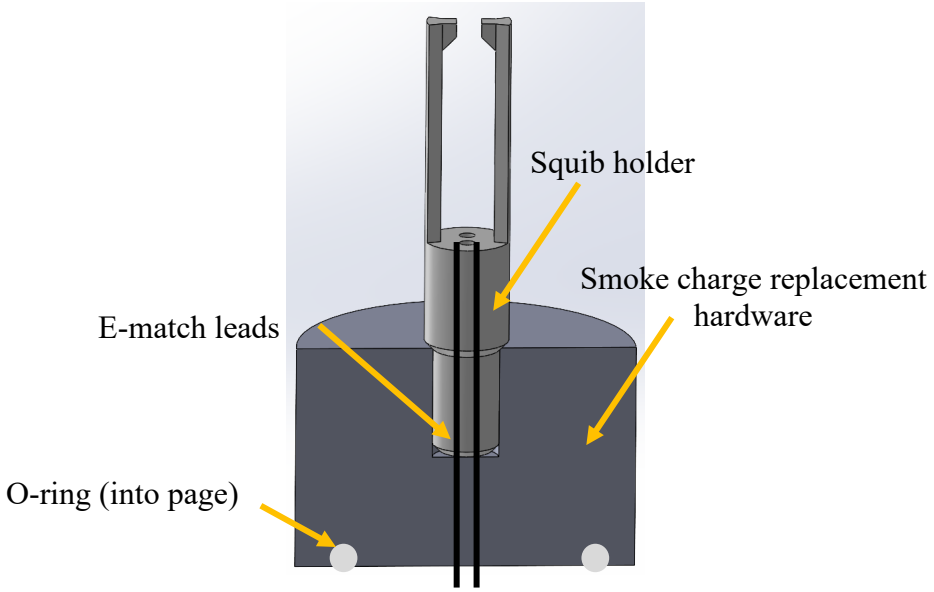

Figure 33. 3D model of squib holder within smoke charge replacement puck

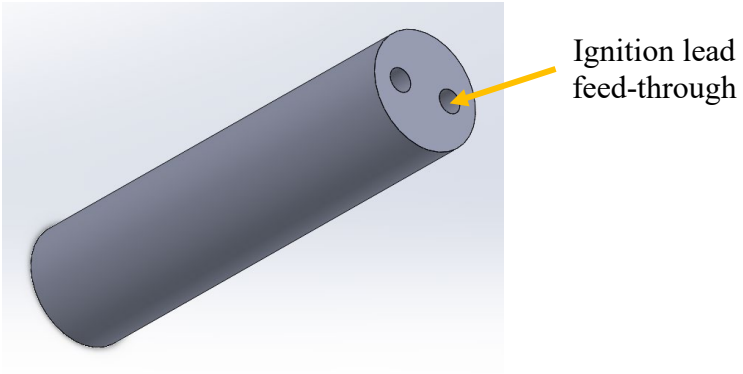

Figure 34. Vacuum chamber test article

The final design of the squib holder is shown in Figure 35. The holder expanded into a larger diameter after emerging from the smoke charge replacement puck via a filleted section that was designed to wedge into the hole in the puck as pressure rose in the motor chamber, improving the sealing mechanism. The long supports are meant to pinch the squib in place and provide support during the booster-phase vibration. The thin supports were designed to quickly melt and be expelled from the chamber.

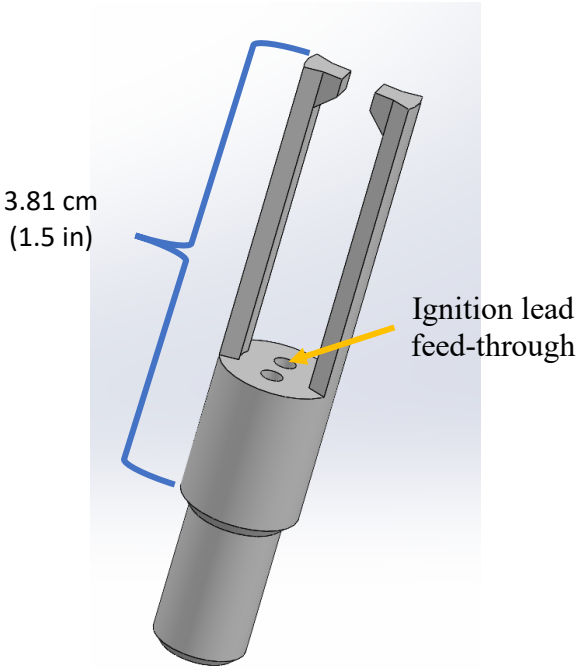

Figure 35. Ignition squib holder final design

B. NOZZLE ENCLOSURE SYSTEM

The primary driving requirements for the design of the nozzle enclosure system were the needs for reliable blowout at the desired pressure and to create a hermetic seal under storage conditions for propellant longevity. Maintaining a complete seal once the propellant began to burn, however, was not as important so long as the system maintained the ability to rapidly pressurize.

After observing the performance of the polycarbonate squib basket under combustion conditions, polycarbonate was again chosen as the material with which the nozzle enclosure would be 3D printed. As the entirety of the enclosure system existed aft of the nozzle throat, there was no concern about throat blockage. The ability for the material to withstand high temperature and force for a short duration with minimal distortion was desirable.

The system consisted of two parts—a retainer and the nozzle enclosure that had an O-ring contact with the nozzle surface and was ejected at the desired pressure. Because there was intended to be no or minimal escape of gas through the nozzle, the pressure initially pressing on the nozzle enclosure was treated as equal to the stagnation pressure within the motor chamber.

1. Nozzle Enclosure Plug

The initial design for the nozzle cap considered a plug that contacted the internal surface in the supersonic (diverging) portion of the nozzle versus an external cap that fits around the nozzle. Figure 36 depicts a generic converging-diverging (CD) nozzle.

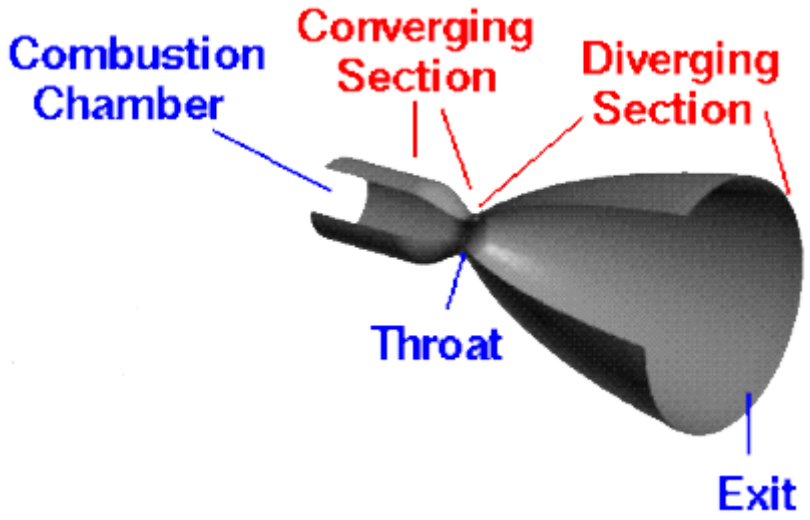

Figure 36. Geometry of a converging-diverging (CD) nozzle. Source: [17].

The major benefit to the plug design, an example of which is pictured in Figure 37, was that it allowed for the precise control of the force required to eject the plug at the desired blowout chamber pressure. The pressure surface, in this case, was the projected 2D surface created by the O-ring seal. This is due to the fact that all radial components of the force acting normal to the plug surface are cancelled out as a result of the plug's axisymmetric design.

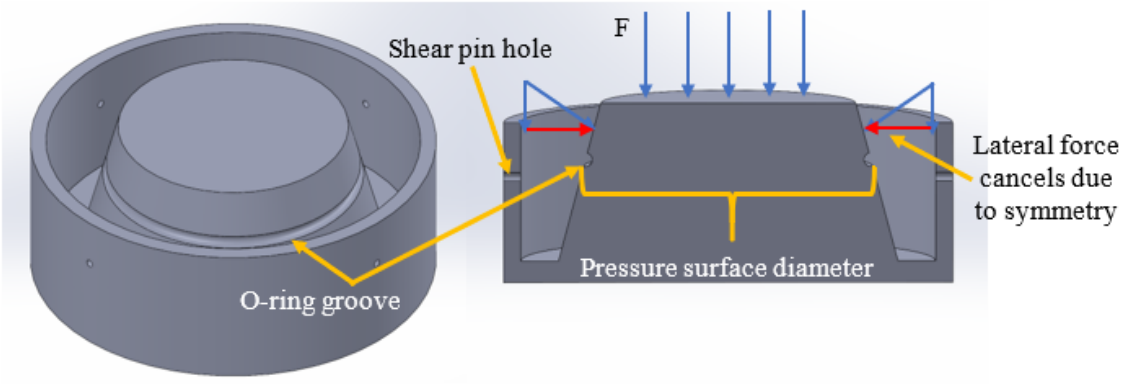

Figure 37. Plug cap 3D model

The design of the plug, however, required meticulous measurement of the geometry of the COTS nozzle to be used. This limited motor selection for the sustainer phase to the motors for which the RPL had the hardware on-hand. The design shown in Figure 37 was based on the nozzle for the Cesaroni M3400 98mm SRM. Once the plug shape was modeled, the location and size of the O-ring was determined using the following equation, where $D_{O\text{-}ring}$ is the O-ring seal diameter, F is the force at which the failure mechanism releases the plug, and P is the motor chamber gauge pressure at blowout.

$$D_{O-ring} = 2\sqrt{\frac{F}{\pi P}} \tag{3}$$

For testing purposes, F was set at 222.4 N (50 lbf) and P was set to 103.4 kPa (15 psi). The O-ring groove was, therefore, placed at the location on the plug where the diameter was 5.232 cm (2.06 in).

2. Nozzle Enclosure Cap

The benefit of an enclosure cap that fits around the exterior of the COTS nozzle was that it offered a much more modular design that was agnostic to the internal geometry of the specific nozzle. The cap enclosure system could theoretically be used with any nozzle of the same diameter with only minimal adjustments made to the enclosure retainer based on the extent to which the nozzle protruded from the motor case. Figures 38a and 38b show examples of a recessed and a protruding nozzle, respectively. This modularity greatly improved motor selection possibility. The cap design also required far fewer nozzle measurements. Only the outer diameter and protrusion of the nozzle was needed. This reduced risk of a compromised seal due to imperfect enclosure fit and allowed for the design of caps for nozzles that were not on-hand.

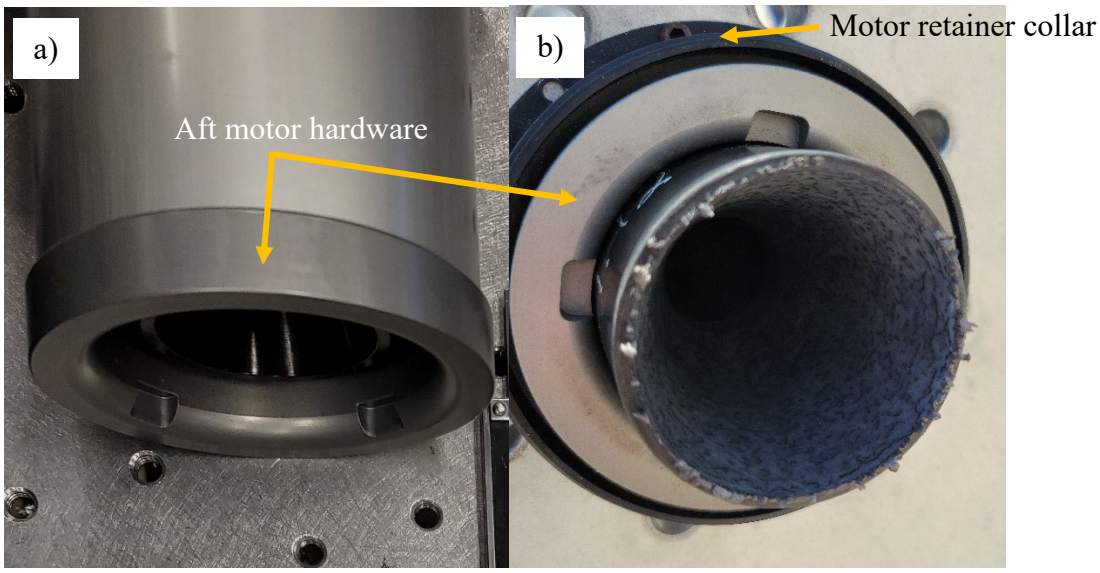

Figure 38. Example of a) recessed and b) protruding nozzles

Because the O-ring in the cap design made contact with the outer surface of the nozzle, the pressure face was determined by the nozzle exit area plus the thickness of the nozzle walls. In the case of the Cesaroni M1540 75mm SRM, for which the cap shown in Figure 39 was designed, the pressure face had an area of 15.9 cm^2 (2.46 in^2).

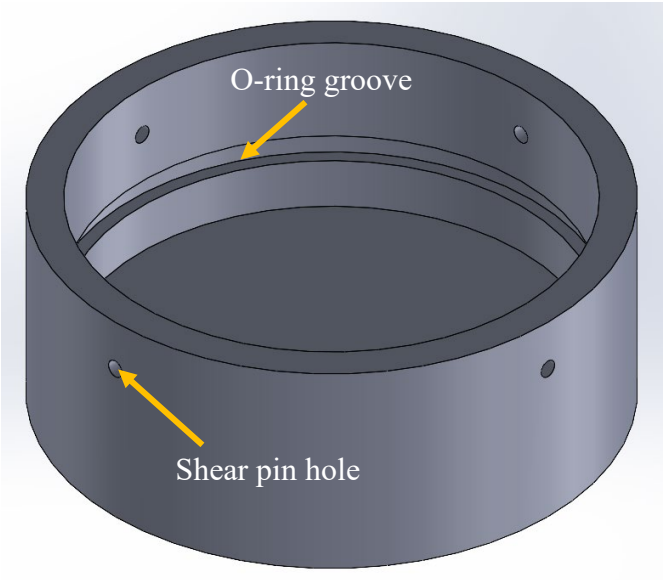

Figure 39. Nozzle enclosure cap 3D model

3. Enclosure Retainer

An enclosure retainer that included a 3D-printed arm, which was intended to bolt on to the aft bulkhead of the rocket and hold the enclosure in place, was briefly considered. Figure 40 depicts the positioning of the arm in relation to the enclosure plug/cap.

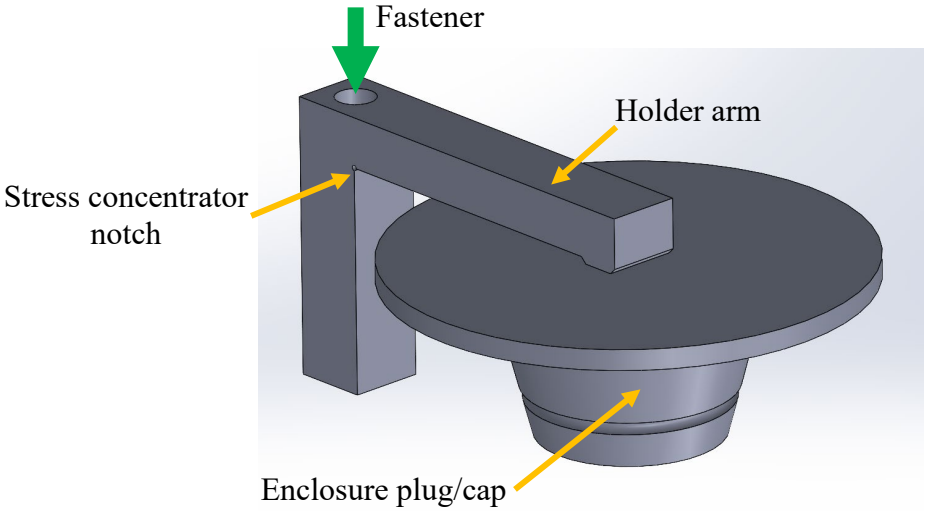

Figure 40. Enclosure retainer arm and plug/cap

The intent was for the arm to contact the center of the plug/cap. The force of the pressure acting on the cap was transferred along the arm to a stress concentrator notch that acted as the failure point. Polycarbonate was chosen as the printing material due to its high brittleness. Despite this, laboratory strength testing caused a significant amount of bending in the arm prior to failure. The strength testing was conducted by hanging increasingly heavier weights from the end of the arm. The holder was fastened to a sturdy table in a manner representative of the way in which it would be fastened to the bulkhead of a rocket.

It was determined that the flex in the arm would allow the enclosure plug/cap to tilt to one direction, which would have allowed a significant escape of gas prior to blowout. Additionally, designing to a specified failure force proved to be a tedious and imprecise process of trial and error, with each print taking approximately eight hours to complete. Because of these issues, the arm design was ultimately abandoned in favor of a more

reliable securing method involving commercial nylon shear pins which failed in a more repeatable manner.

Experimentally obtained shear limits of #2 nylon pins in various configurations are provided in Table 2. Average peak load for a configuration with two shear pins was 109.6 N (24.64 lbf) with a standard deviation of 6.51 N (1.46 lbf). Configurations of three and four shear pins averaged 95.24 N (21.41 lbf) and 95.01 N (21.36 lbf), respectively. Of note, the standard deviation of the final failure loads decreased as the number of pins is increased. Three and four-pin configurations had standard deviations of 4.48 N (1.01 lbf) and 4.28 N (0.96 lbf), respectively, revealing that as the number of shear pins increased, the system became less sensitive to the defects and differences of individual pins.

Table 2. Shear limits of #2 nylon pins. Adapted from [18].

#2 Nylon Screws				
# of Pins	**Peak Load in N (lbf)**		**Peak Load (Each Pin)**	
2	236.3	(53.12)	118.1	(26.56)
2	204.4	(45.95)	102.2	(22.98)
2	226.2	(50.85)	113.0	(25.42)
2	230.4	(51.80)	115.2	(25.90)
2	213.2	(47.92)	106.6	(23.96)
Avg	**222.1**	**(49.93)**	**109.6**	**(24.64)**
3	278.6	(62.64)	92.88	(20.88)
3	269.4	(60.57)	89.81	(20.19)
3	286.4	(64.40)	95.50	(21.47)
3	277.6	(62.41)	92.52	(20.80)
3	305.9	(68.76)	102.0	(22.92)
3	296.4	(66.64)	98.79	(22.21)
Avg	**285.8**	**(64.24)**	**95.24**	**(21.41)**
4	385.7	(86.70)	96.39	(21.67)
4	386.4	(86.86)	96.57	(21.71)
4	350.4	(78.77)	87.59	(19.69)
4	374.9	(84.27)	93.72	(21.07)
4	380.8	(85.62)	95.19	(21.40)
4	402.1	(90.40)	100.5	(22.60)
Avg	**375.6**	**(84.44)**	**95.01**	**(21.36)**

Figure 41 shows an exploded 3D cutaway view of the concept for the shear pin retainer and cap. Each component was drilled with symmetrically-spaced holes for the shear pins. The retainer took the shape of a collar that fit around the outer surface of the COTS nozzle. The cap fit between the nozzle and the collar such that the shear pin holes in the cap and the collar aligned. The collar was designed to fit within the existing motor retaining hardware without the need for any modification to the aft bulkhead.

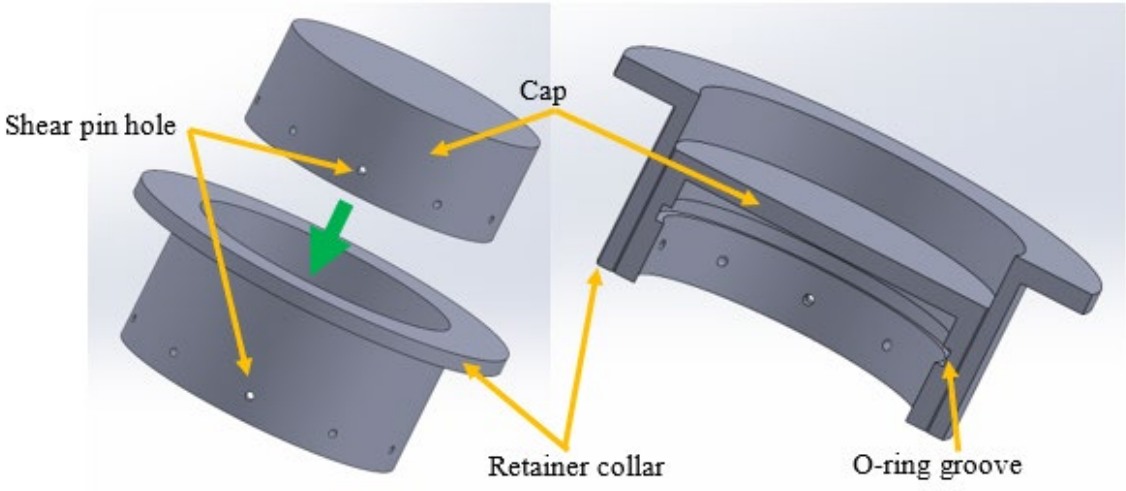

Figure 41. Shear pin retainer collar and cap

C. BLAST TUBE

The proposed blast tube design was based on the estimated geometry of the Cesaroni O8000 150 mm rocket motor. The O8000 was selected because it offered the highest thrust from a COTS motor that fit within the existing RRPD-V body. It was the largest available COTS SRM, providing more than 8,007 N (1800 lbf) of initial thrust and was "originally designed to boost a [227 kg (500 lb)] experimental cruise missile to flight speed" [19]. Because of its diameter, the O8000 precluded the use of aft fin control servos in the RRPD-V without incorporation of a blast tube.

The final blast tube geometry would be dependent on the constraint imposed by the size of the servos needed to control the aft fins of the rocket. Other size and weight

characteristics of the RRPD-V at the time of design should also be considered to ensure the shift in CG that results from incorporating the blast tube could be favorable. What should remain constant within the design, however, is that the inner port diameter should remain larger than the nozzle throat diameter. The blast tube was, thus, designed foremost around this parameter. Because the COTS O8000 motor nozzle was not available to be measured, the geometry had to be estimated. Based on information provided by CTI, the nozzle throat was estimated to have a diameter of 3.0 cm (1.2 in). Measurements taken from the nozzle of an M3400, which used the same White Thunder propellant mixture as the O8000, were used to estimate the O8000 nozzle expansion ratio. The O8000 propellant grains were estimated to have an initial inner diameter of 5.08 cm (2 in). This diameter was also used as the inner blast tube diameter forward of the nozzle. Figure 42 shows a 3D model of a blast tube designed to fit into the existing O8000 motor case. The shape was intended to be able to replace the existing COTS nozzle without any modifications to the motor case. Figure 43 depicts how the blast tube would fit into a fully-assembled O8000 motor.

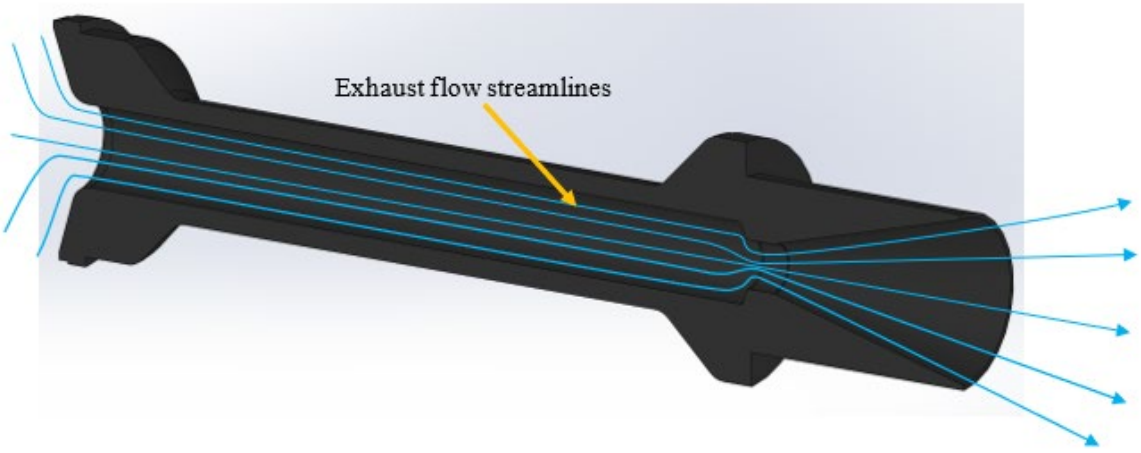

Figure 42. 3D model cutaway of blast tube based on the O8000 motor

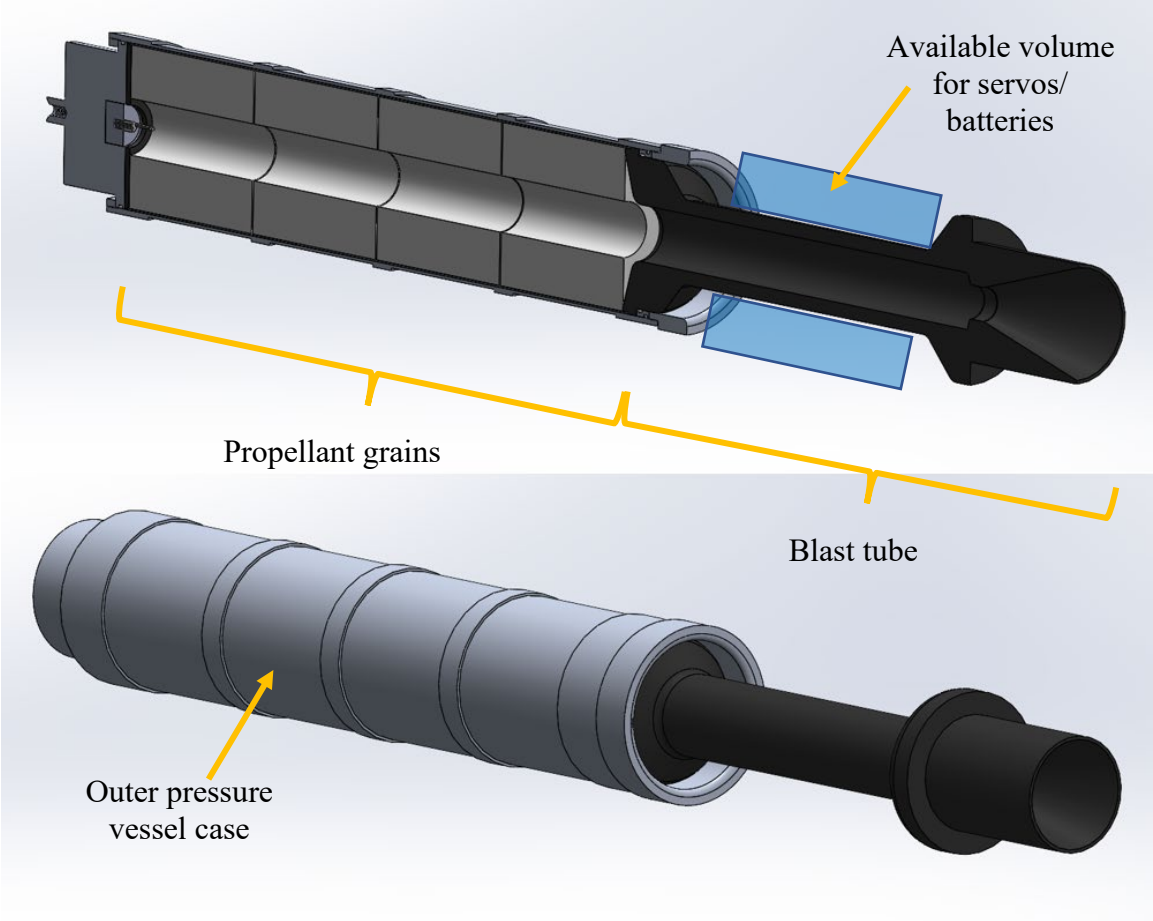

Figure 43. 3D model of blast tube assembled into O8000 motor

A common practice in amateur solid propellant rocketry is to machine nozzles out of solid micro fine-particle graphite rod. These rods, however, become exceedingly expensive as diameter increases. The size of rod needed to machine a blast tube for a 150 mm diameter motor would need to be special ordered and would cost thousands of dollars. An alternative method of manufacture is to wrap carbon-phenolic tape around a mandrel that is pre-machined to the desired geometry of the blast tube. The NASA Marshal Space Flight Center (MSFC) described this manufacturing process:

> The carbon cloth used to fabricate composite solid rocket motor nozzles is impregnated with the binder or matrix prior to wrap and cure. This preimpregnated material is commonly called “prepreg” in the composite industry. The diversity of the manufacturing process requires six different vendors before final material is produced. These vendors: 1) produce rayon thread; 2) weave cloth; 3) carbonize cloth; 4) produce resin; 5) produce

> carbon fillers; and 6) impregnate carbon cloth with resin and filler (production of prepreg). Constant monitoring of all phases of the manufacturing process is required to ensure satisfactory quality. The rayon thread is manufactured, then woven into cloth 60 in. wide. The rayon cloth is carbonized by slowly heating to 1000 deg. to 1500 deg. C in an inert atmosphere. Critical factors to be controlled in this process are the rate of temperature increase, time, and maintenance of an inert atmosphere in the oven.
>
> After carbonization, the carbon-cloth is impregnated by drawing it through a heated container of phenolic resin and carbon filler to form prepreg. Critical factors that must be carefully controlled in the preimpregnation process are temperature of the resin/filler mixture, tension and speed of the cloth through the resin/filler mixture, pressure on the roller to ensure penetration of resin into the cloth, oven temperature after impregnation to remove volatiles, and control staging of the resin. [20]

MSFC also described the tape wrapping process. In the case of the blast tube, the mandrel would likely need to consist of at least two sections; one for the converging portion of the tube/nozzle and one for the diverging section.

> The tape wrapping process places the tape at the proper angle and debulks the tape material to minimize movement of the tape during cure. Debulking of the tape should be achieved by applying heat and pressure at the point of contact with the mandrel or the previous ply. Heat should be applied prior to wrapping to make the tape tacky. The pressure roller forces the fibers to nest and compact (debulk) within the resin/fabric matrix. CO2 is used to cool the resin to stop further cure, and dimensionally and thermally stabilizes the billet for further processing…After wrapping, the billet and mandrel are vacuum bagged for waterproofing, then installed in a hydroclave for final cure. Curing of the carbon-cloth liner requires a pressure of 1000 psi at 310 deg. F for a minimum of five hours. After the cure cycle, a test ring should be removed and tested to verify the properties of the cured carbon cloth phenolic. The carbon cloth is then machined to configuration. [20]

Additional layers of phenolic tape could then be wrapped by first applying a coat of phenolic resin to the previous layer. At each consecutive stage, the component should be vacuum-bagged and cured at a pressure of 1.72 MPa (250 psi) and a temperature of 154 °C [20]. Table 3 lists the properties of the cured carbon phenolic wrap at room temperature unless otherwise stated.

Table 3. Cured material physical and mechanical properties of carbon phenolic. Adapted from [20].

Property		Limits	
		Minimum	**Maximum**
Density (g/c^3)		1.4	1.52
Resin content (%)		30.0	38.5
Compressive strength (MPa), edgewise	Wrap direction	172	448
	Fill direction	138	379
Interlaminar double sheer strength (MPa)		24	55
Thermal conductivity (W/m-K) @ 121 °C	Across ply	0.17	1.9
	With ply	0.17	1.9
Coefficient of thermal expansion ($1/°K \times 10^{-6}$) @ 204 °C	Across ply	9.0	36.0
	With ply	3.6	16.2
Flexural strength (MPa)	Wrap direction	172	379
	Fill direction	138	379
Tensile strength (MPa), edgewise	Wrap direction	103	276
	Fill direction	68.9	241

THIS PAGE INTENTIONALLY LEFT BLANK

IV. EXPERIMENTAL RESULTS

A. STATIC MOTOR LIVE-FIRE TESTING

One of the goals of the static live-fire test was to record the thrust and chamber pressure of a motor with both the head-end ignition system and aft nozzle enclosure in place. To accomplish this, a pressure transducer was connected through the forward retaining hardware of an M3400 motor using Swagelok tubing. The chamber pressure of the motor was not provided by the manufacturer, so a conservative approach was taken in selecting the pressure transducer. In order to avoid transducer saturation, a 20.7 MPa (3000 psi) transducer was selected. The same thrust stand that is pictured in Figure 28 was used for this test.

The data from the live fire are graphically depicted in Figures 44, 45, and 46. A fair amount of 60 Hz electronic noise was present in the testing equipment and needed to be filtered out. To do this, the raw data .tdms files were converted to Microsoft Excel spreadsheets and imported into Matlab. The data were then run through a band stop IIR filter and adjusted for the offset imposed by the data acquisition equipment. Figures 44 and 45 depict the data before and after filtering for pressure and thrust, respectively.

The phase shift between the measured pressure and thrust data was due to the extra processing time incurred as a result of the conditioning electronics through which the load cell voltages were processed and amplified. The rise in thrust was otherwise expected to correlate temporally to the rise in pressure. This could also explain the more gradual rise and drop of the experimental pressure curve compared to that of the manufacturer-provided curve shown in Figure 47. The measured average thrust was 3505 N. This was on the order of what was expected, given the manufacturer-provided average thrust of 3421 N [21].

Interestingly, the pressure curve more closely resembled the manufacturer-provided thrust profile than did the experimental thrust curve. Again, this was likely an artifact of the conditioning electronics. At any rate, the correlation between the chamber pressure and the thrust was expected, given the relationship in Equation 4, where T is thrust, $\dot{m}$ is the mass flow out of the motor, v_e is the flow exit velocity, P_e is the pressure at the

exit of the nozzle and is directly tied to chamber pressure, P_o is ambient environmental pressure, and A_e is the nozzle exit area. $\dot{m}$, v_e, and A_e can be assumed nearly constant for a neutral burn profile.

$$T = \dot{m}v_e + (P_e - P_0)A_e \tag{4}$$

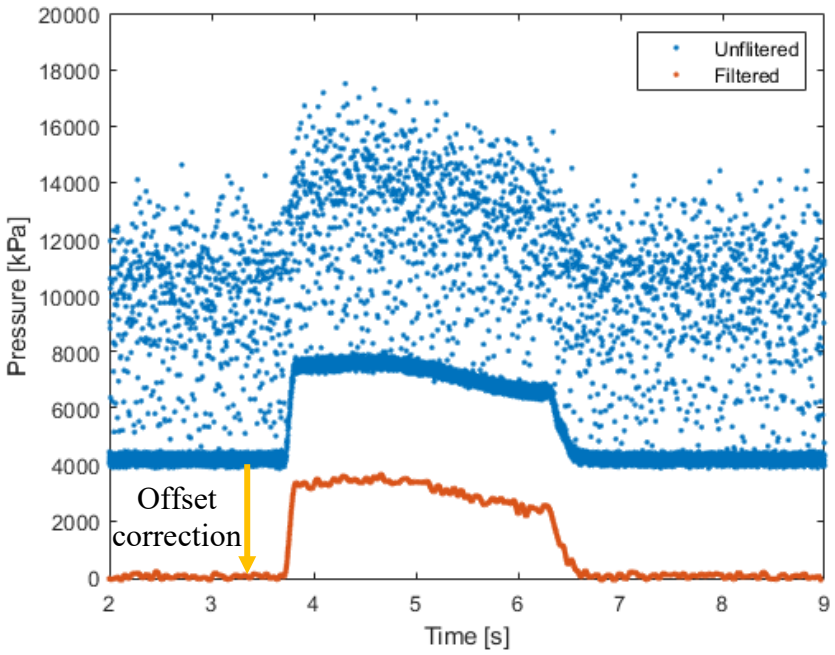

Figure 44. M3400 chamber pressure vs. time

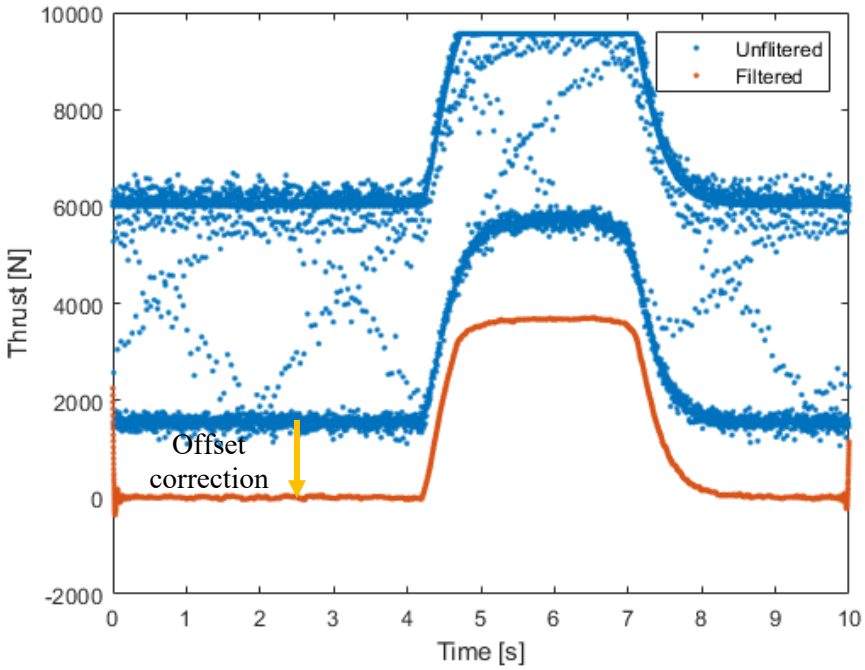

Figure 45. M3400 thrust vs. time

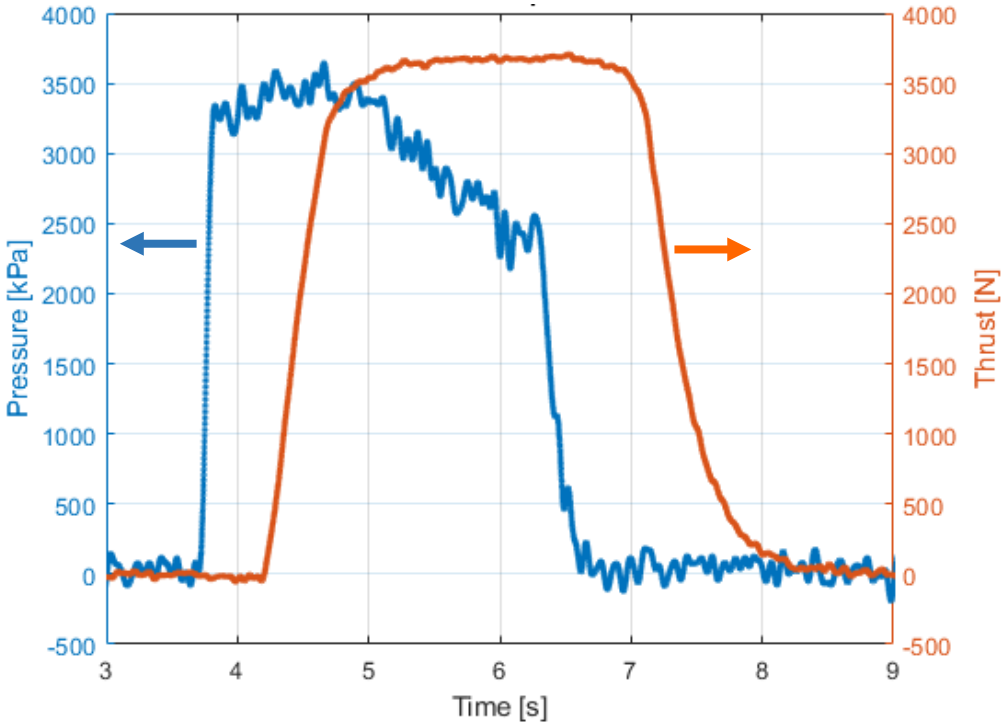

Figure 46. M3400 pressure and thrust profiles

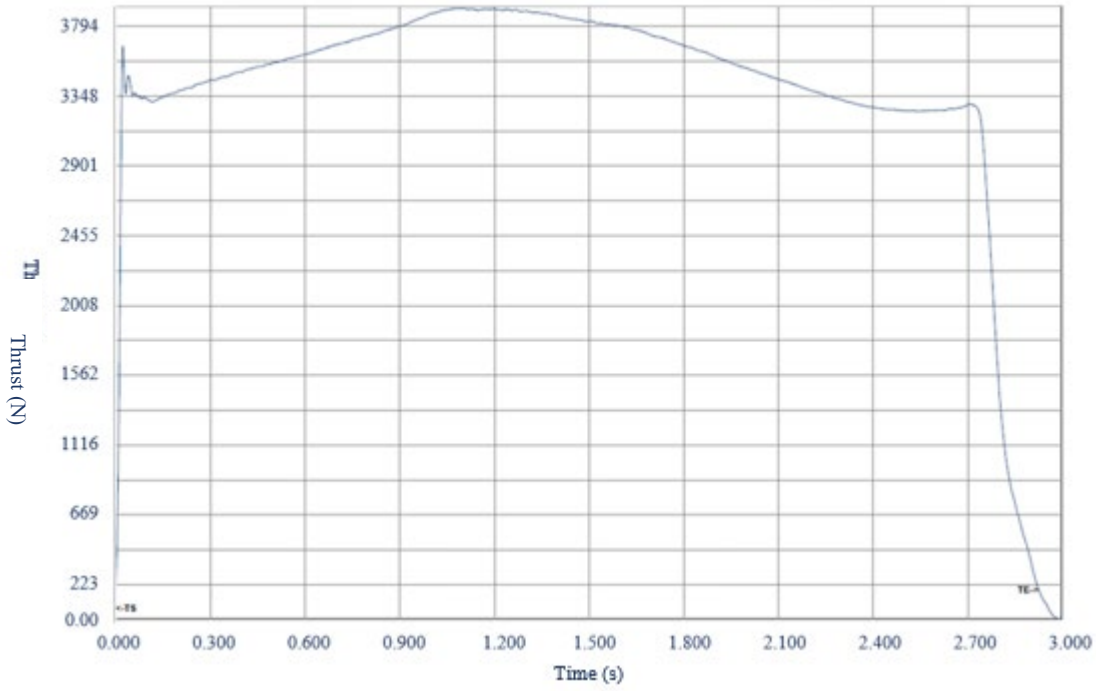

Figure 47. M3400 representative thrust curve. Adapted from [21].

The expected pressure response was a profile close to what is circled in green in Figure 48. The pressure was expected to rise sharply to the blowout pressure, drop slightly with the expulsion of the nozzle enclosure, then rapidly climb to maximum pressure. However, the response highlighted in Figure 48 fell within the 1% uncertainty associated with the pressure transducer. It was, therefore, impossible to make a conclusion about the performance of the nozzle enclosure from these data. What was able to be gleaned, however, was the range of chamber pressure that could be expected in subsequent firings. This informed the selection of pressure transducers for follow-on tests to ensure the expected nozzle enclosure blowout pressure fell outside of the uncertainty of the transducer while also avoiding saturating the transducer.

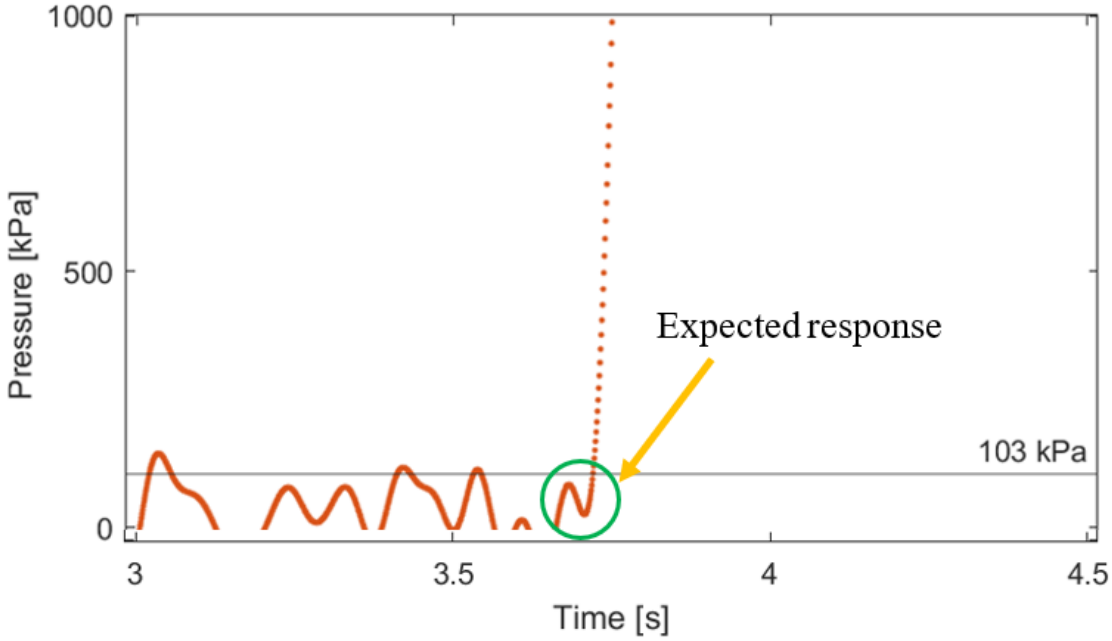

Figure 48. Zoomed in M3400 pressure vs. time

B. NOZZLE CAP LABORATORY TESTING

Laboratory testing of the nozzle cap consisted of two parts—the firing of a squib inside a known closed volume and shear pin blowout tests. The closed volume squib test was conducted first to determine the pressure increase created by just the ignition of the squib. Swagelok tubing and fittings were used to create a volume representative of an M1540/M1400 75 mm motor chamber. A squib was sealed into one end, and a 6895 kPa (1000 psi) pressure transducer was fixed to the other. Figure 49 shows the test article. Figure 50 shows a graphical representation of the data obtained from the pressure transducer. A peak gauge pressure of 120.9 kPa was achieved. This value was used to inform the baseline pressure that the nozzle cap needed to withstand in order to avoid premature blowout, assuming no initial mass addition from burning propellant.

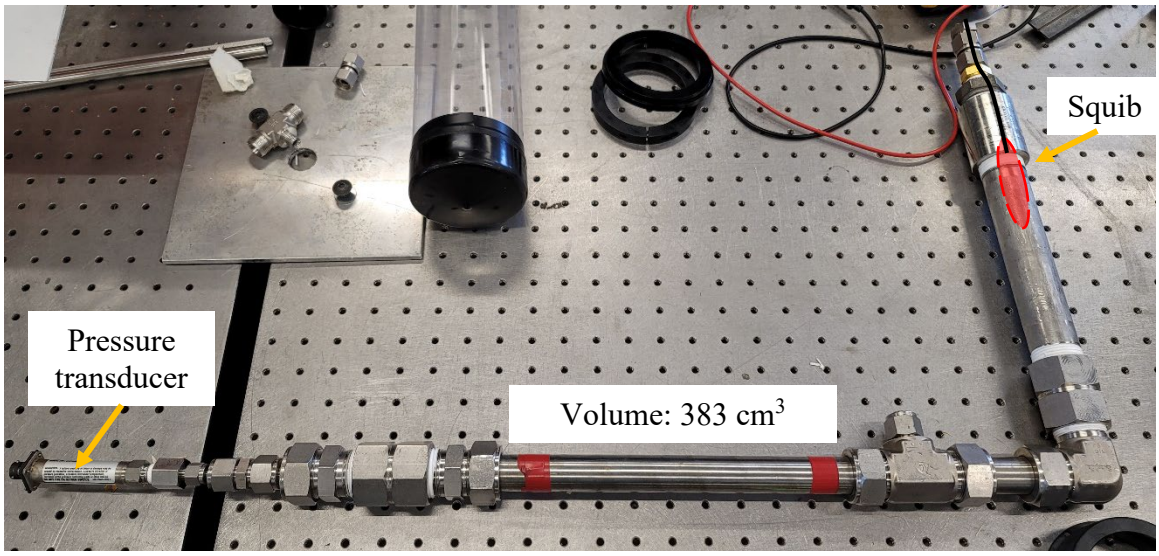

Figure 49. Enclosed squib test apparatus

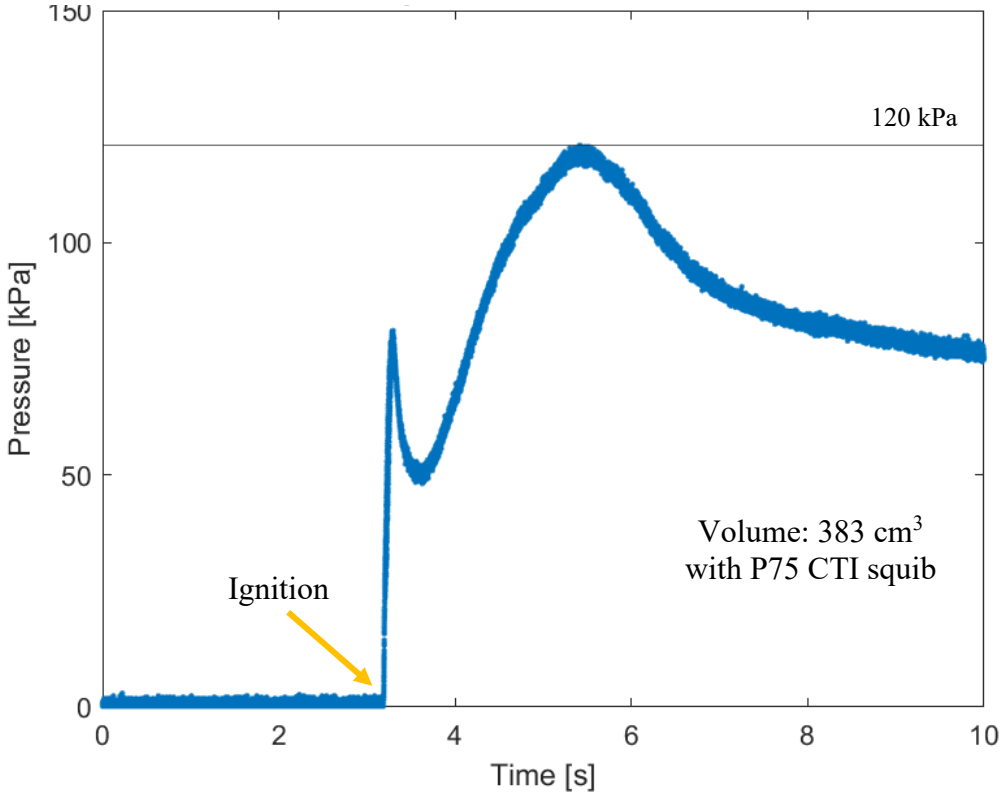

Figure 50. Enclosed squib test pressure vs. time

A subsequent test involved securing an enclosure cap to a motor assembly as it would be installed during ground or flight testing, excluding propellant or a squib.

Compressed air was then rapidly fed through the forward end of the motor case through tubing that was also connected to a pressure transducer. This was done for two and four pin configurations. The test configurations were restricted to even pin counts to ensure load symmetry. Figure 51 depicts the setup of the forward end of the test apparatus.

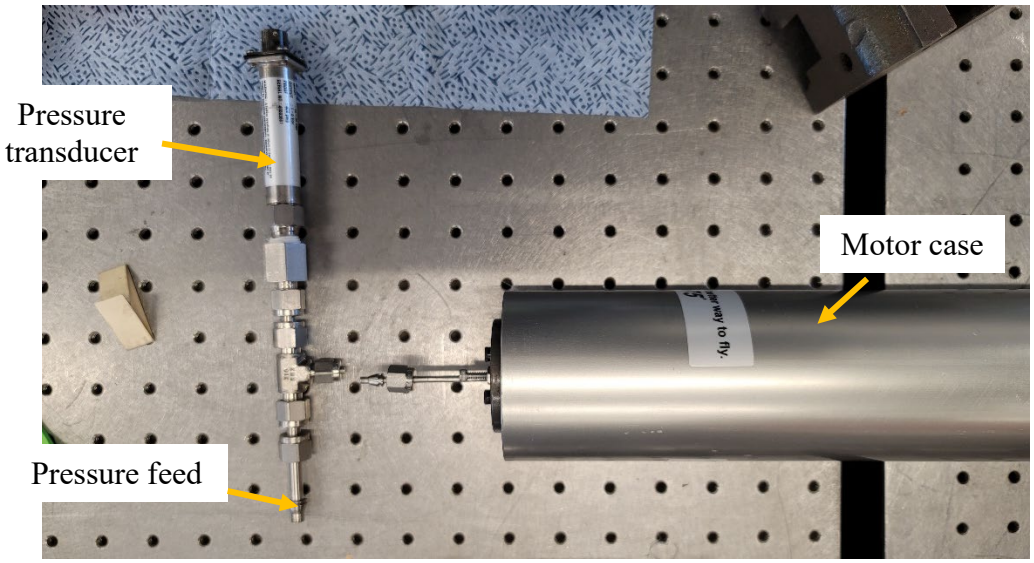

Figure 51. Nozzle cap test apparatus

The results of these tests are graphically depicted in Figures 52, 53, and 54. In each of these figures, the blowout pressure is marked by a black horizontal line and labeled with the pressure value. Although the pressure transducer shown in Figure 51 did locally measure transient pressures slightly above the blowout pressure, the ultimate point of cap blowout was clearly represented by a sharp drop in pressure to 0 kPa. The four pin configuration withstood up to 354.5 kPa, while the six pin configuration withstood on average 821.5 kPa. The pressures represented FS margins over the base squib ignition pressure of 2.93 and 6.79, respectively. Both configurations were, therefore, acceptable in terms of achieving a margin outside of the transducer's 1% uncertainty. The four pin configuration was selected for follow-on flight testing in an effort to mitigate the risk of inadvertently extinguishing the propellent. The slope of the pressure drop off in Figure 52 was noted to help identify the expected pressure response, referenced in Figure 48, for follow-on tests.

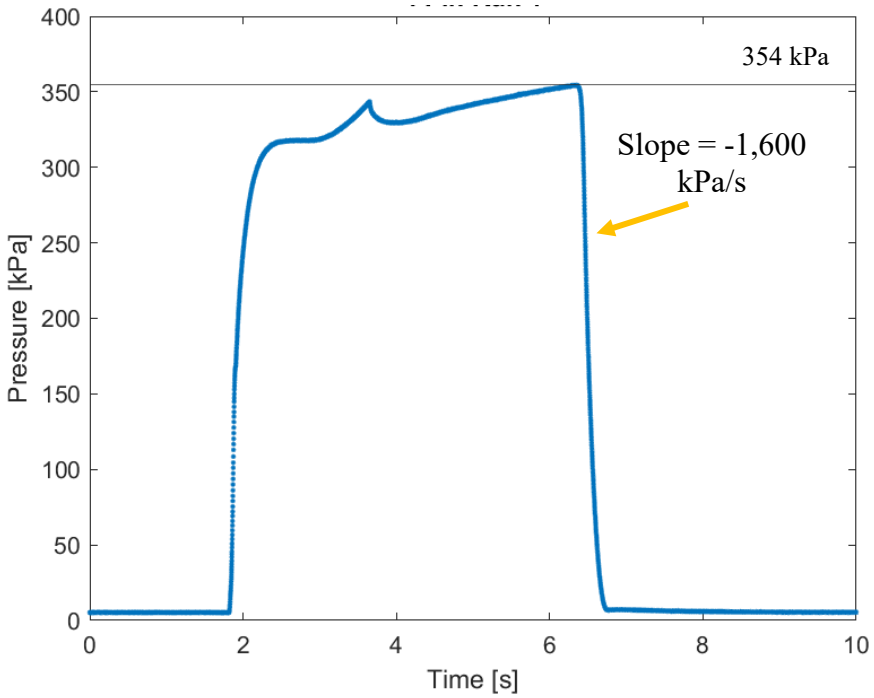

Figure 52. Four pin nozzle cap/test run 1 pressure vs. time

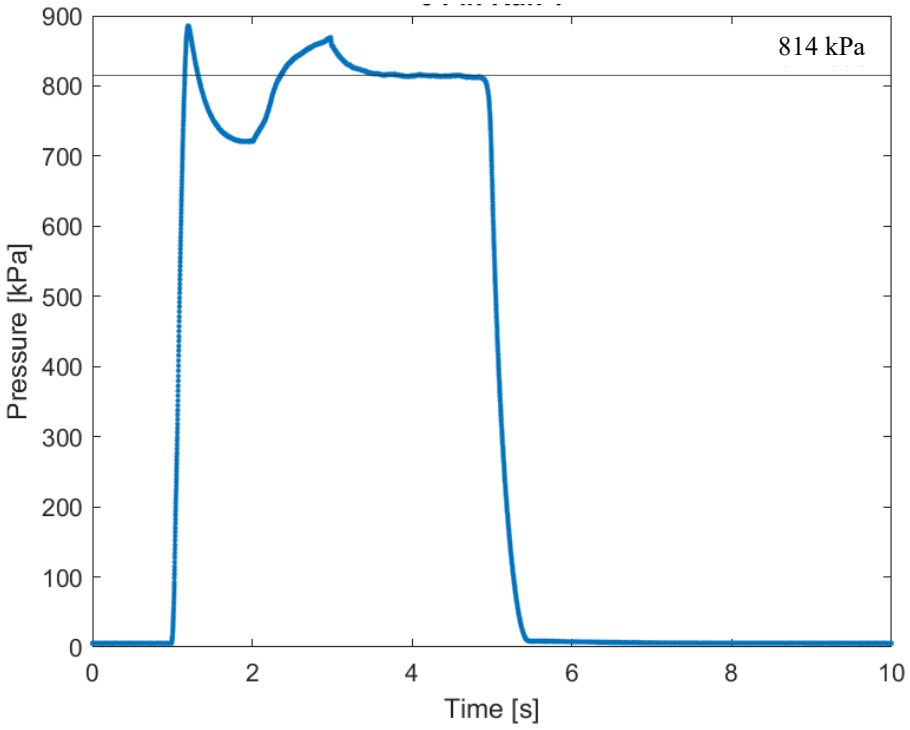

Figure 53. Six pin nozzle cap/test run 1 pressure vs. time

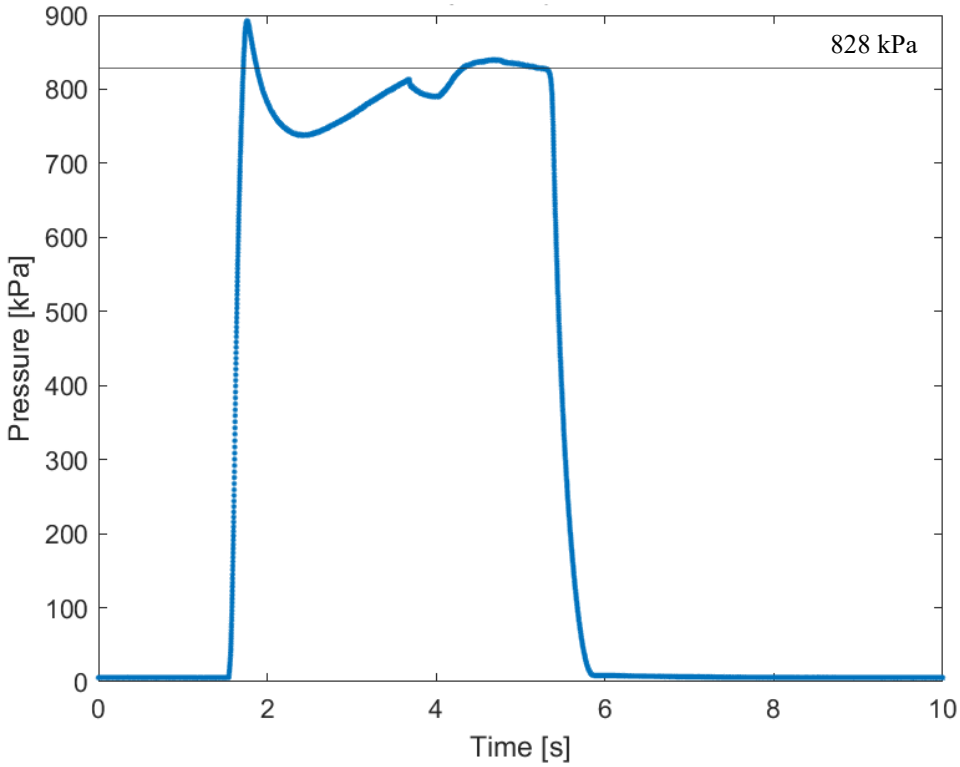

Figure 54. Six pin nozzle cap/test run 2 pressure vs. time

THIS PAGE INTENTIONALLY LEFT BLANK

V. ROCKET FLIGHT TESTING

A. OCTOBER 2021 TWO-STAGE ROCKET

1. Rocket Vehicle Design

The rocket utilized in this study was separate from the RRPD-V. It was a two-stage, unguided solid propellant rocket that acted as a test platform for the SRM modifications developed in this study. The purpose of the October 2021 launch was to demonstrate the ability of the head-end ignition system to autonomously ignite the second stage SRM with an installed nozzle cap under flight conditions. OpenRocket was used to model the rocket prior to construction to evaluate the stability and flight characteristics of the proposed design. The OpenRocket software was also used to develop the shape, size, and placement of the booster and sustainer fins. The final OpenRocket model is depicted in Figure 55.

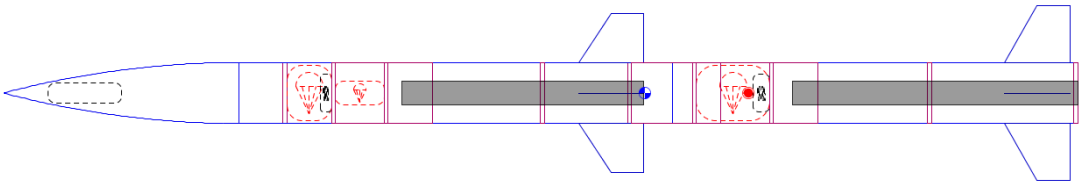

Figure 55. OpenRocket model of rocket design

A minimum stability threshold of 0.95 cal was set for each stage of the rocket. By manipulating the fin sweep angle, sweep length, tip chord, and position, suitable stability margins of 1.7 cal for the booster phase and 0.96 cal for the sustainer phase were achieved for crosswinds up to 5 m/s. The rocket fins were cut from 0.300 cm (0.118 in) thick fiberglass sheet and were limited to a span of 17.8 cm (7 in). This limitation was due to the size of the fiberglass sheets available. Additionally, larger fin sizes complicated storage considerations. Figure 56 shows the booster body components.

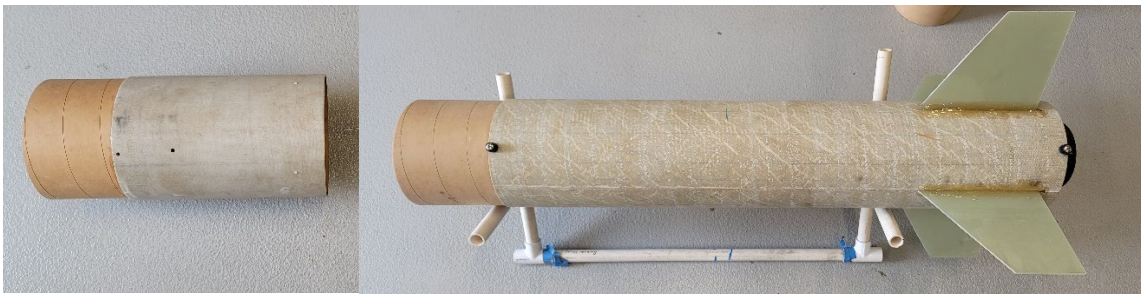

Figure 56. First stage booster (right) and parachute bay (left)

The booster section of the rocket consisted of a 96.52 cm (38 in) tube that was connected to a 30.48 cm (12 in) interstage section that housed the parachute bay and the booster flight electronics. The interstage section slid over an overlapping coupler that extended from the booster tube and was secured with four #2 nylon shear pins. The electronics bay was situated forward of the booster engine block and segregated by 1.27 cm (1/2 in) wooden bulkheads on either side. Between the electronics bay and the booster engine block was the booster parachute bay. The booster was designed to carry most 98 mm diameter motors and included an adapter sleeve, pictured in Figure 57, to accommodate smaller 75 mm motors, such as the M2075 used in this launch. Figure 58 depicts the OpenRocket model of the sustainer section of the RPV.

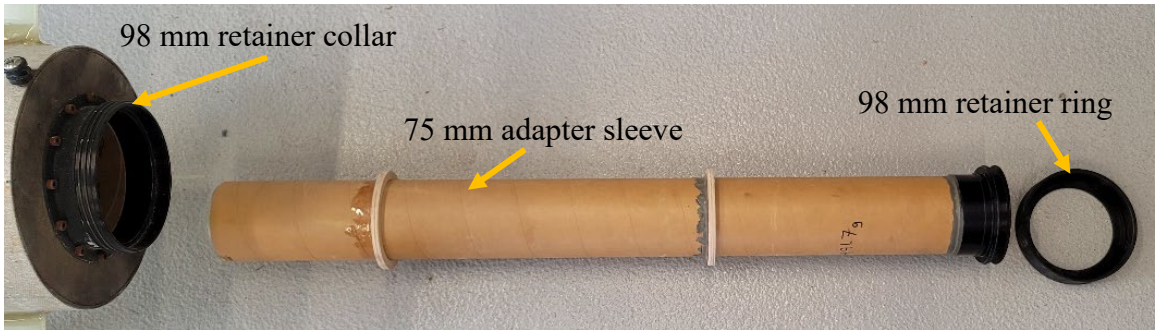

Figure 57. Booster motor adapter sleeve

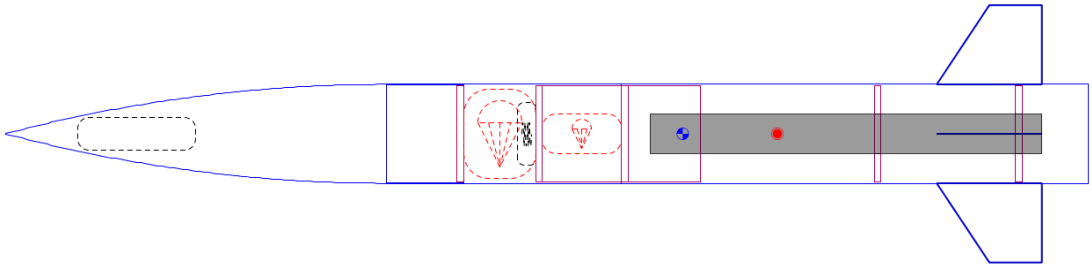

Figure 58. OpenRocket sustainer section model

The sustainer section consisted of an 85.09 cm (33.5 in) tube that held the second stage motor, a 75 mm M1400 in this case. A 45.40 cm (17.875 in) section of tube forward of the sustainer motor housed the drogue parachute, the sustainer electronics bay, and the sustainer main parachute. Forward of the parachute bay tube was the nose cone.

The main rocket body was built out of 19.05 cm (7.5 in) diameter phenolic cardboard tube wrapped in a fiberglass shell. The coupler tubes were made of 18.65 cm (7.343 in) diameter phenolic cardboard tubes. The nose cone was stock fiberglass with a gel-coat surface. Figure 59 shows the sustainer motor section.

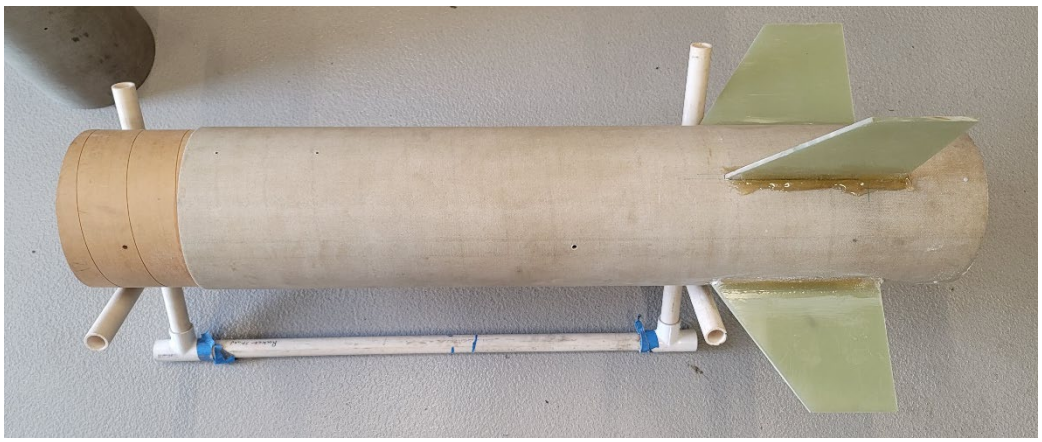

Figure 59. Sustainer motor section

Simulations ran with OpenRocket for the design pictured in Figure 55 generated an expected apogee for the sustainer of 4,027 m (13,213 ft) above ground level and a

maximum speed of 335 m/s (1100 ft/s), or Mach 0.99. Figure 60 shows the OpenRocket graphical representation of the simulation for the sustainer section of the rocket.

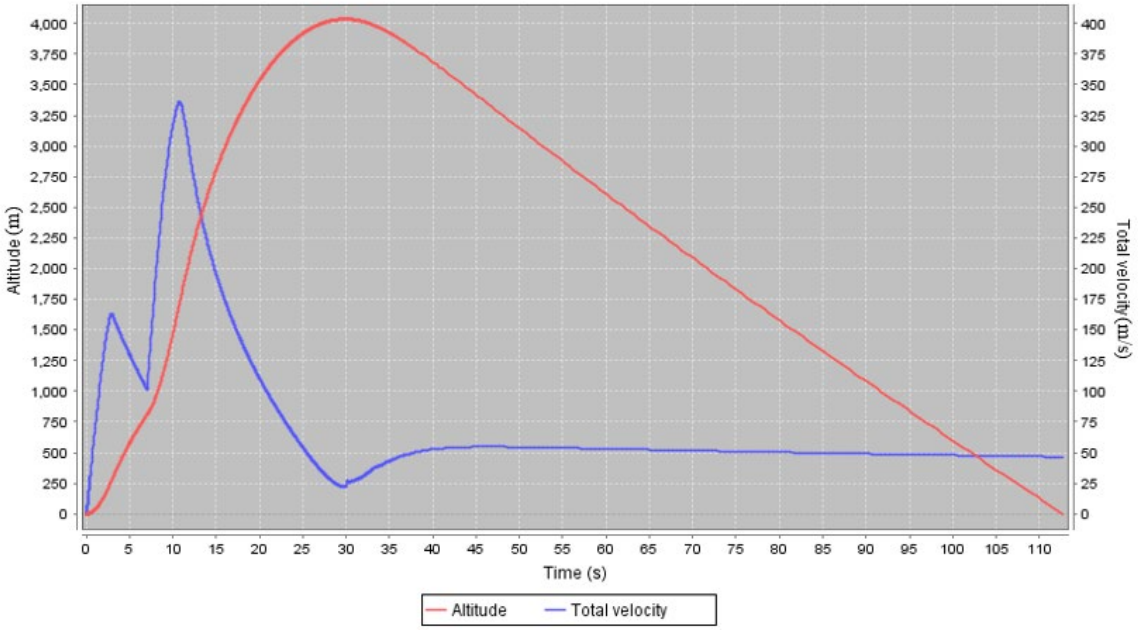

Figure 60. OpenRocket simulation sustainer for October 2021 rocket launch

2. Flight Electronics

The rocket booster used an Altus Metrum TeleMega altimeter for telemetry recording and parachute deployment. A PerfectFlite StratoLoggerCF altimeter was used as a backup. Each altimeter was powered individually by separate 9V batteries. The TeleMega recorded height, speed, acceleration, and vertical acceleration for the boost phase of the flight, whereas the StratoLoggerCF recorded just altitude and temperature. These components are pictured in Figures 61 and 62.

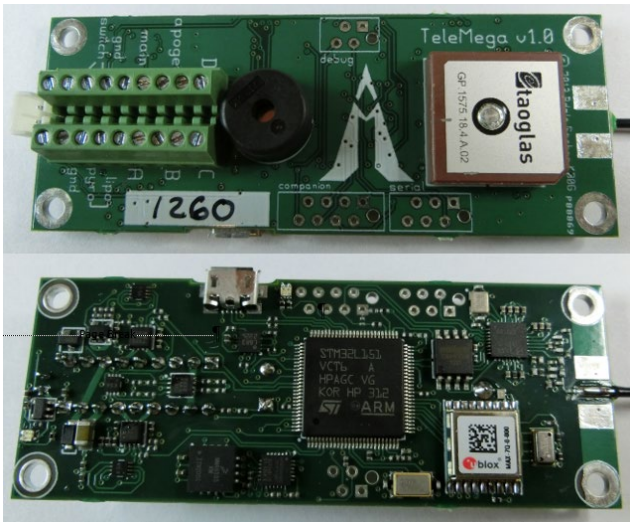

Figure 61. Altus Metrum TeleMega. Source: [22].

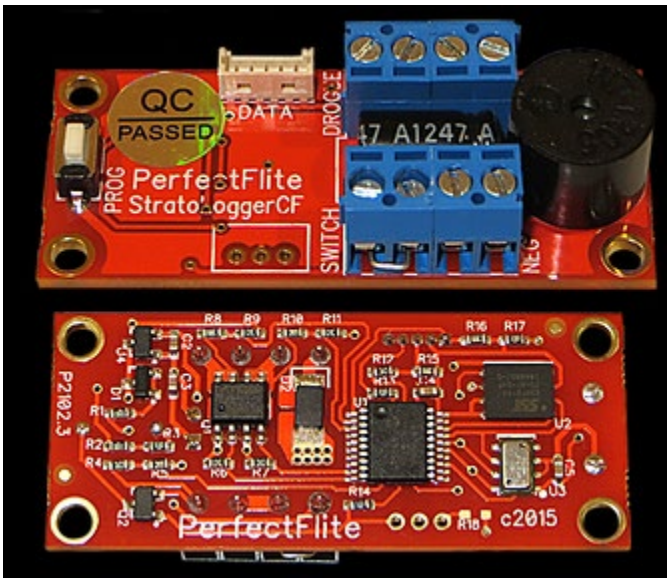

Figure 62. PerfectFlite StratoLoggerCF. Source: [23].

The TeleMega and the StratoLoggerCF were each connected to E-matches that initiated black powder charges within the booster parachute bay as pictured in Figure 63. The ignition of the black powder created enough pressure within the compartment to shear the pins securing the interstage section to the booster, releasing the booster parachute in the process.

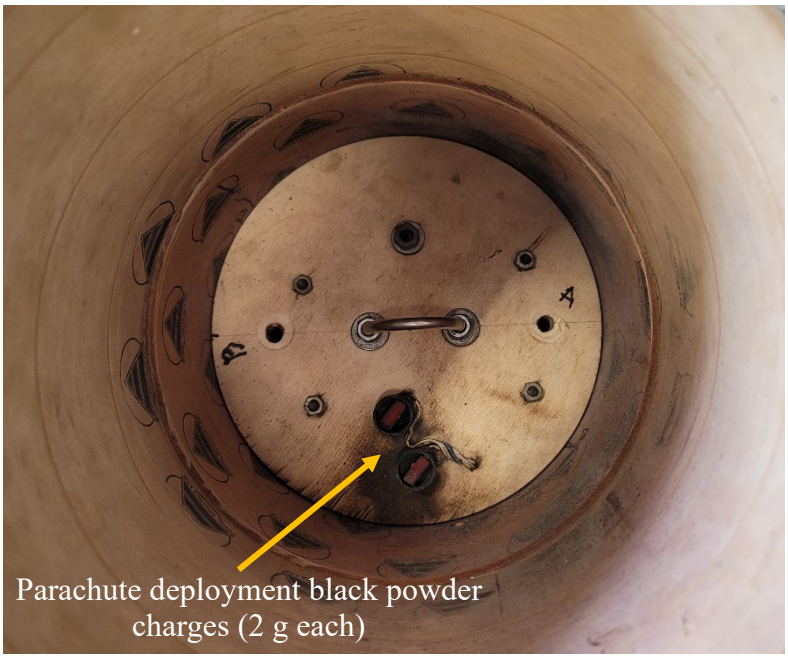

Figure 63. Internal view of booster parachute bay and aft electronics bulkhead

The sustainer flight electronics included two Altus Metrum EasyMega altimeters, pictured in Figure 64, for redundancy. Again, each altimeter was powered by a 9V battery, and each recorded height, speed, acceleration, and vertical acceleration. These EasyMegas were used to control stage separation, sustainer ignition, sustainer drogue parachute deployment, and sustainer main parachute deployment.

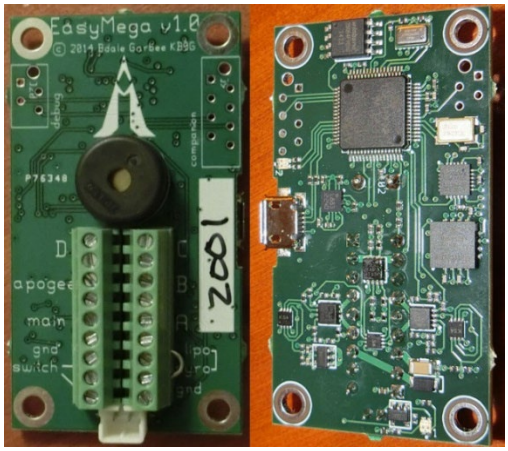

Figure 64. Altus Metrum EasyMega. Source: [24].

Because the sustainer section of the rocket was expected to reach a much higher apogee than the booster, a drogue parachute was included to reduce the time aloft and the subsequent recovery distance. The drogue allowed the rocket body to fall at a reduced velocity until a specified altitude was reached, at which point the main parachute was deployed. Two separation charges were utilized. E-match leads were fed through a tube that ran the length of the sustainer motor section to a black powder charge on the outside of the forward booster electronics bay bulkhead, shown in Figure 65. The other E-match lead from the EasyMega was fed through the sustainer engine block bulkhead to the head-end ignition system. These leads were connected to the sustainer electronics bay via barrel jacks, as shown in Figure 66, to allow for quick disconnection during drogue parachute deployment. A CO2 separation charge was used for the drogue parachute deployment since the altitude at which the drogue deploys precludes the use of black powder due to reduced reactivity.

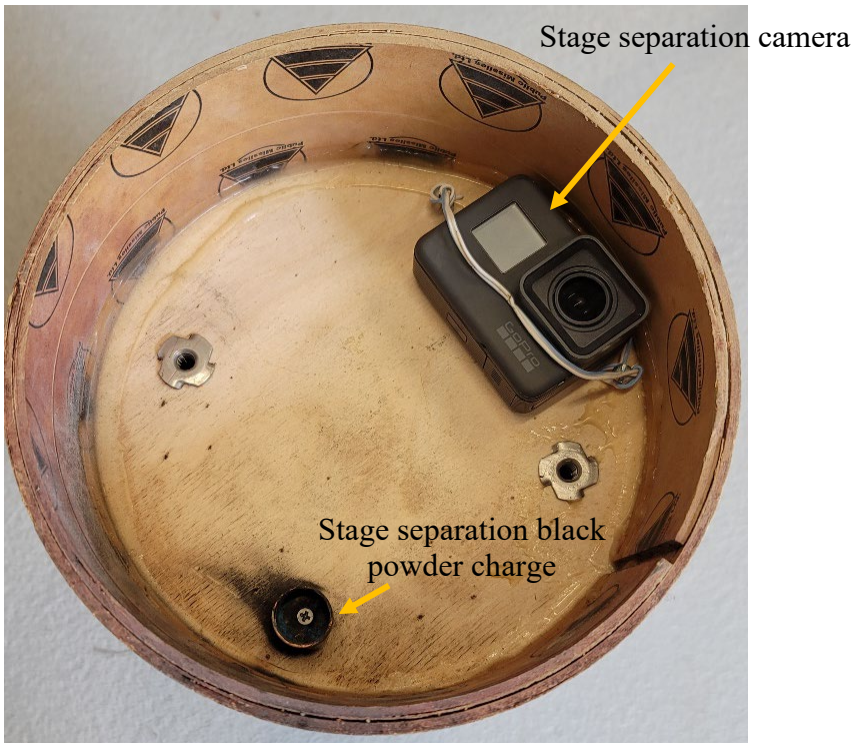

Figure 65. Booster electronics bay forward bulkhead

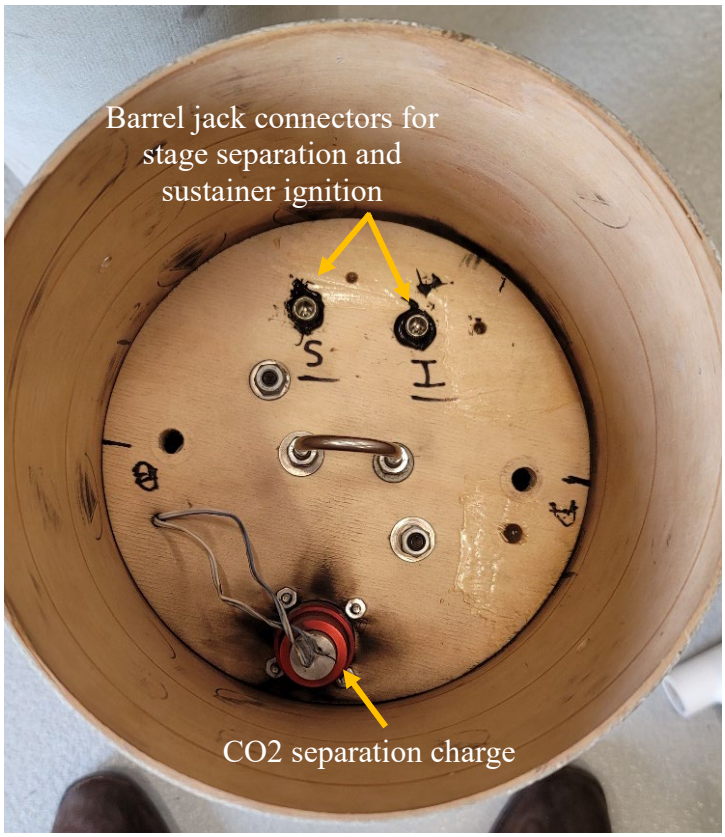

Figure 66. Internal view of drogue parachute bay and sustainer electronics bay aft bulkhead

The final electronic component in the sustainer was the Multitronix Kate-1 TelemetryPro Transmitter, shown in Figure 67, that was housed in the nose cone. Kate-1 was a self-contained flight data recorder and transmitter that operated on a one-watt 900 MHz signal [25]. Figure 68 shows an exploded view of all the components of the sustainer electronics bay and nose cone.

Figure 67. Multitronix Kate-1 TelemetryPro transmitter. Source: [25].

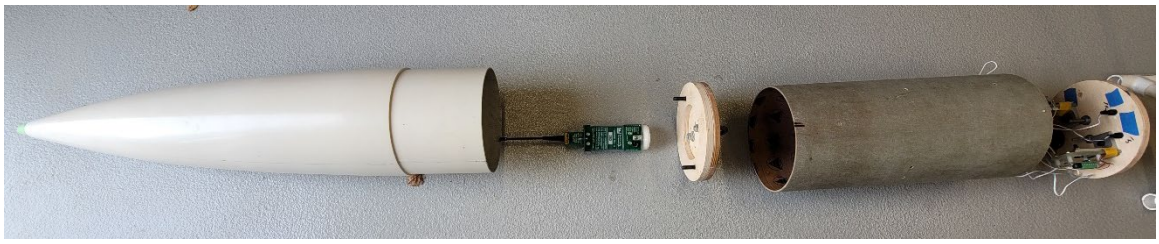

Figure 68. Sustainer electronics bay and nose cone exploded view

3. Flight Data and Results

This flight incorporated the head-end ignition and the nozzle enclosure systems into the sustainer portion of the rocket. Although there was no pressure monitoring system aboard this flight, there were two cameras onboard that captured the stage separation and sustainer motor ignition. Video from the onboard cameras as well as video captured from the ground confirmed successful second stage ignition. Both stages were successfully recovered with minimal damage and no loss of flight data.

Table 4. Booster flight statistics

Maximum height	936.8 m / 3073 ft	
Maximum speed	164.9 m/s / 541 ft/s / Mach 0.5	
Max boost accel	106.9 m/s^2 / 351 ft/s^2 / 10.90 G	
Avg boost accel	62.0 m/s^2 / 204 ft/s^2 / 6.33 G	
Ascent time	2.6 s boost	7.4 s coast
Main descent rate	8.5 m/s / 28 ft/s	
Descent time	83.2 s	
Flight time	93.2 s	

The booster stage functioned as expected and had a burn time of about three seconds, followed by a two-second coast prior to stage separation. After an apogee of 936.7

m (3073 ft), the booster section fell under free fall to a height of 600.0 m (1969 ft), at which point the main parachute was released. Figure 69 shows a graphical representation of booster acceleration, height, and speed over time.

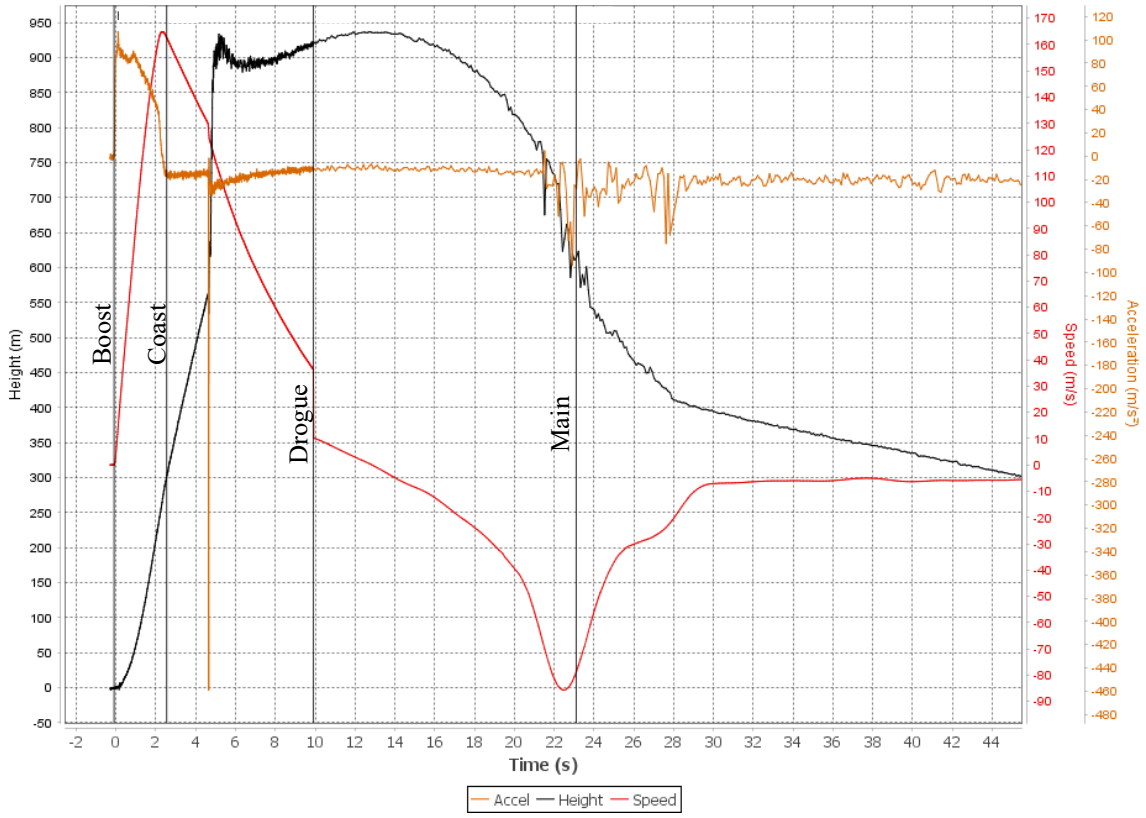

Figure 69. Booster stage flight data

Figures 70 and 71 show stills before and after stage separation, indicating successful staging. Figure 72 shows a still taken from the video captured by the camera mounted on the outside of the forward booster electronics bay bulkhead shortly after stage separation occurred. It shows the white nozzle enclosure cap in place on the sustainer motor.

Figure 70. Booster stage burn

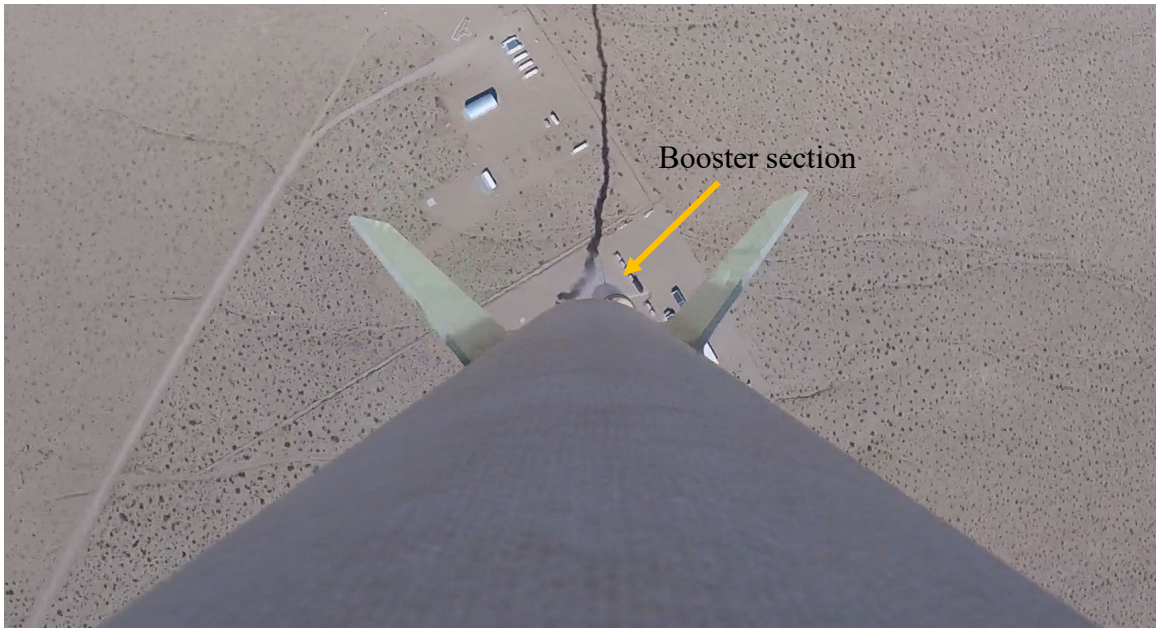

Figure 71. Moment of separation

Figure 72. Sustainer after stage separation

The external aft-facing camera captured the moment that the head-end ignition system fired. The next frame of the video revealed that the nozzle cap was ejected at that time as a result of the pressure build from only the ignition of the squib. Figure 74 shows still frames from these two points. It took nearly four more seconds for the propellant to fully light and for the sustainer to enter its boost phase.

The nozzle cap was secured to the collar with two shear pins for an expected shear force of 222 N (50 lbf) based on Table 2. This equated to a total pressure of 131 kPa (19 psi). Because of the elevation change between the launch site, where the motor chamber was sealed, and the height at sustainer ignition, the change in pressure from elevation $\Delta P_{elevation}$ needed to be accounted for when calculating the chamber pressure for cap blowout $P_{c\,(blowout)}$.

$$P_{c\,(blowout)} = \frac{F_{shear} n_{pins}}{A_{cap}} - \Delta P_{elevation} \tag{5}$$

In Equation 5, F_{shear} is the average shear force per pin, n_{pins} is the number of pins, and A_{cap} is the area of the pressure surface. Atmospheric pressure could be estimated prior to launch by linearly interpolating data from Table 5. Flight data recorded on the

EasyMega, however, provided more accurate pressure readings. Figure 73 depicts the atmospheric pressure data recorded by the sustainer. At launch, the atmospheric pressure was 94.0 kPa (13.6 psi). At squib ignition, indicated by the red line labeled "Squib ignition" in Figure 73, the atmospheric pressure was 85.0 kPa (12.3 psi). This equated to a $\Delta P_{elevation}$ of 9.0 kPa (1.3 psi) and a $P_{c\ (blowout)}$ of approximately 122 kPa (17.7 psi). The delay between the ejection of the nozzle cap and the motor entering the boost phase, as corroborated between the video capture and flight data recording, indicated that two shear pins were not sufficient to withstand the pressure spike created by the ignition of the squib itself. Further testing was needed to determine the minimum number of shear pins needed to withstand the initial increase in pressure.

Table 5. Standard atmosphere properties. Adapted from [26].

Elevation (m)	**Temperature (°C)**	**Pressure (kPa)**	**Speed of Sound (m/s)**
0	15.1	101	340.3
500	11.9	95.5	338.4
1000	8.7	89.9	336.4
1500	5.4	84.6	334.5

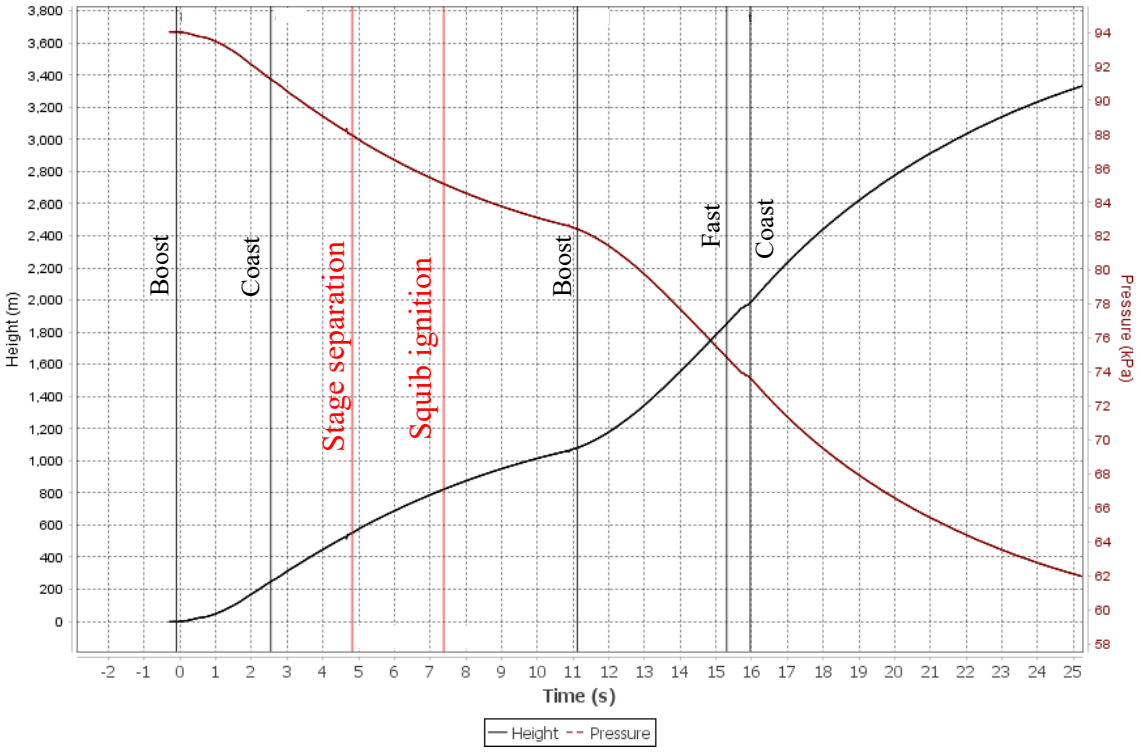

Figure 73. Flight 1 sustainer atmospheric pressure and height data

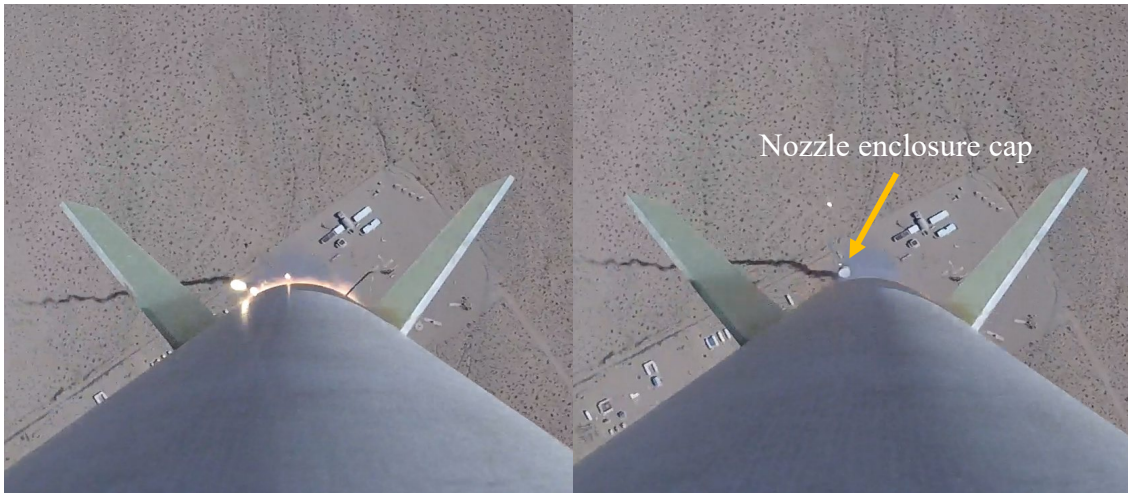

Figure 74. Moment of head-end ignition squib fire

The sustainer portion of the rocket functioned mostly as expected and climbed to a height of 3,670.7 m (12,043 ft). This was on the order of what was expected based on the OpenRocket simulation. It should be noted that OpenRocket was only used as a rough

estimation and not as a rigid performance metric due to the software's underlying analytical model assumptions that can lead to performance variations. One reason why the maximum height may have been less than what was simulated is that the second stage motor did not achieve maximum burn instantaneously. As shown in Figure 75, the motor took about four seconds to reach peak thrust following squib ignition. During this time, the sustainer was losing vertical speed as it decelerated following booster-stage burnout. One of the goals of including the nozzle cap on the sustainer motor was to recapture some of the effective impulse lost during these four seconds while providing a more predictable staging time sequence.

Of particular note in reference to Figure 75 is the very shallow decline in height following where drogue deployment is indicated. Visual observation from the ground confirmed that this was due to the premature deployment of the main parachute at the same time. The separation charges fired appropriately, as was indicated by the recorded data and inspection of the charges after recovery. The most likely explanation for the premature deployment was early failure of the shear pins that secured the nose cone to the parachute bay. In this case, four shear pins were used to produce an estimated shear force of 445 N (100 lbf). When the drogue parachute deployed at apogee, the sustainer body likely still had enough momentum that the sudden deceleration caused the shear pins to yield and release the main parachute as well. Although this did not cause a catastrophic failure, it drastically increased the time aloft of the sustainer. This resulted in a drift of several miles during the decent and exacerbated recovery efforts. To avoid this problem, more shear pins were needed to secure the parachute bay to the nose cone on follow-on launches.

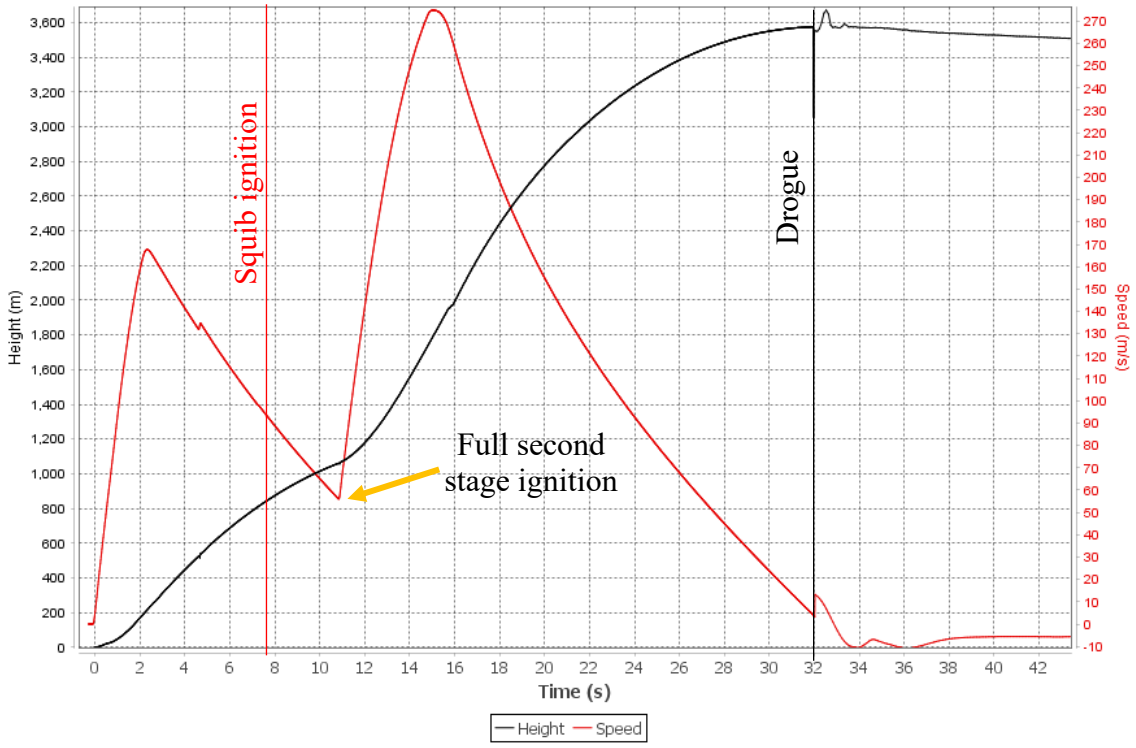

Figure 75. Flight 1 sustainer stage data

Table 6. Sustainer flight statistics

Maximum height	3670.7 m / 12043 ft		
Maximum speed	274.8 m/s / 902 ft/s / Mach 0.8		
Max boost accel	105.6 m/s^2 / 346 ft/s^2 / 10.77 G		
Avg boost accel	55.6 m/s^2 / 182 ft/s^2 / 5.67 G		
Ascent time	6.8 s boost	0.7 s fast	24.6 s coast
Descent rate	7.6 m/s / 25 ft/s		
Descent time	462.9 s		
Flight time	495.0 s		

B. APRIL 2022 TWO-STAGE ROCKET

1. Rocket Vehicle Design

The April 2022 launch was conducted using the same rocket body as the October 2021 launch. Slight repairs were made to the epoxy fillets that secured the fins in place on both the booster and sustainer sections of the rocket. Otherwise, only slight modifications were made to the internal structure to allow a pressure line to feed from the sustainer motor to a new health monitoring system in the sustainer electronics bay.

The M2075 75 mm motor was exchanged for a more powerful M3400 98 mm motor for use as the booster motor. This exchange allowed for the testing of the rocket at faster speeds and greater altitudes as well as for the demonstration of the versatility of the booster body design. The sustainer motor selected for this launch was the M1540 75 mm SRM. The M1540 provided slightly higher impulse than the M1400 used in the October 2021 launch but maintained the same nozzle form factor, preventing the need for a redesign of the nozzle enclosure system. Figure 76 shows the OpenRocket model of the RPV for the second flight.

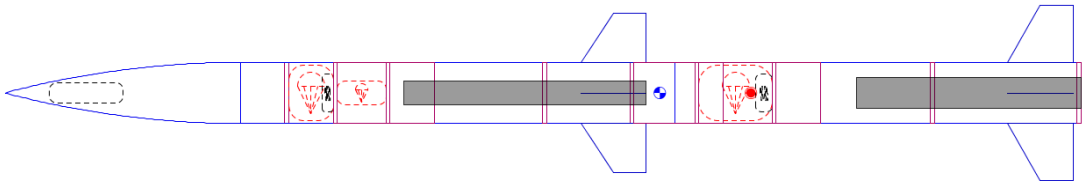

Figure 76. OpenRocket model of April 2022 rocket

OpenRocket simulations generated an expected flight pattern very similar to the October 2021 rocket as shown in Figure 77. The rocket was expected to climb to a new maximum height of 5,000 m (16,400 ft) and achieve a supersonic maximum velocity of 366 m/s (1200 ft/s, Mach 1.1).

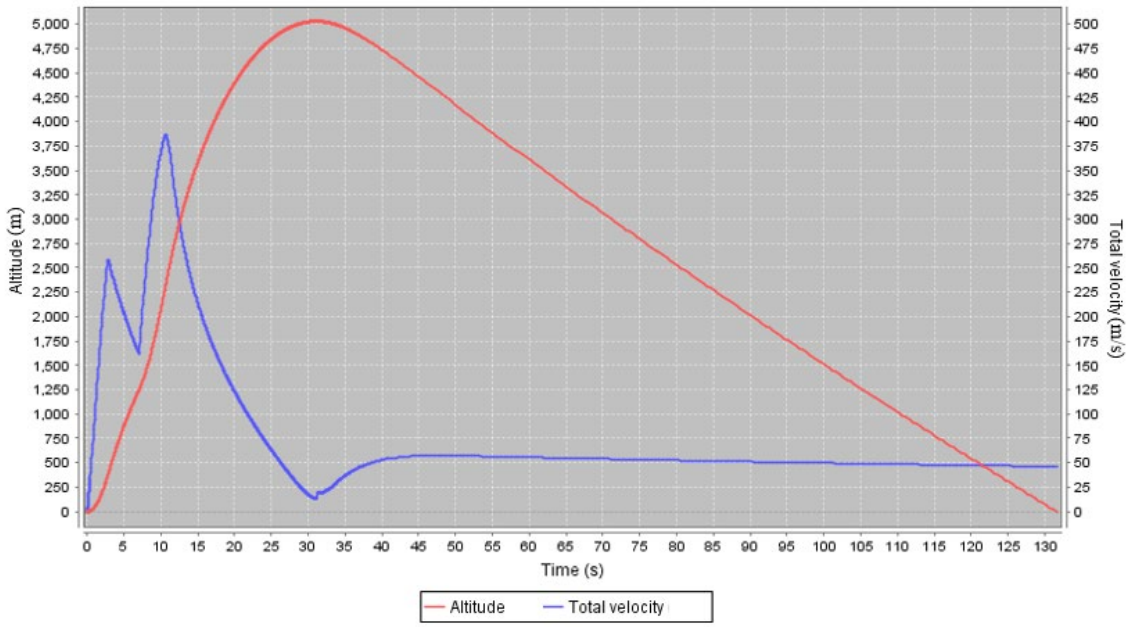

Figure 77. OpenRocket simulated flight for April 2022 rocket launch

2. Flight Electronics

This launch maintained many of the same flight electronics from the previous launch, including the TeleMega and the two EasyMegas. The Kate-1 unit was also kept aboard this flight. The PerfectFlite altimeter in the booster was exchanged for a second TeleMega due to an unknown error that prevented communication with the PerfectFlite when tested during rocket assembly. The major addition to this flight was a modular health monitoring system that consisted of an Arduino UNO microcontroller board and an Adafruit Data Logger Shield, an example of which is pictured in Figure 78.

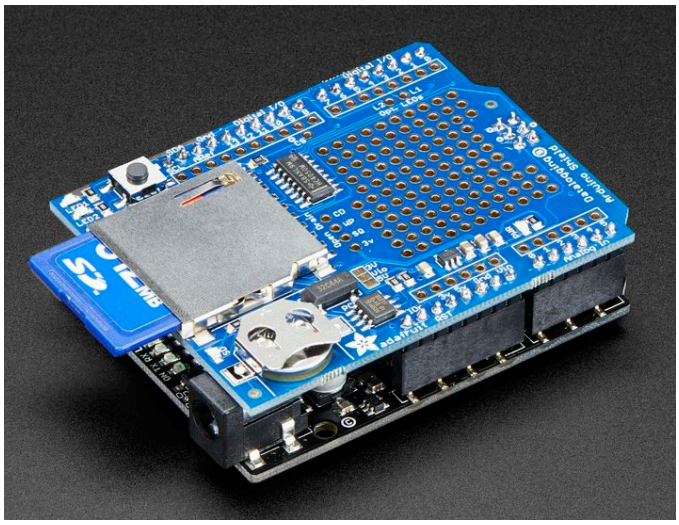

Figure 78. Adafruit Data Logger Shield with Arduino UNO. Source: [27].

The health monitoring system for this flight was set up to read and record inputs from two pressure transducers—one measuring sustainer motor chamber pressure and the other measuring pressure within the drogue parachute bay during separation. The final sustainer electronics bay is shown in Figures 79 and 80.

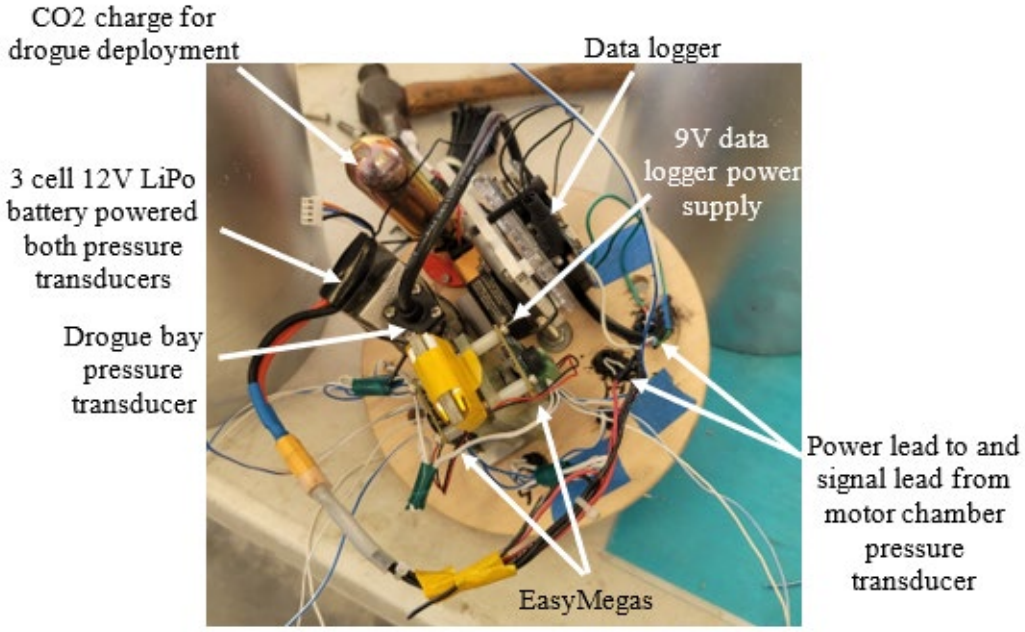

Figure 79. Sustainer avionics bay

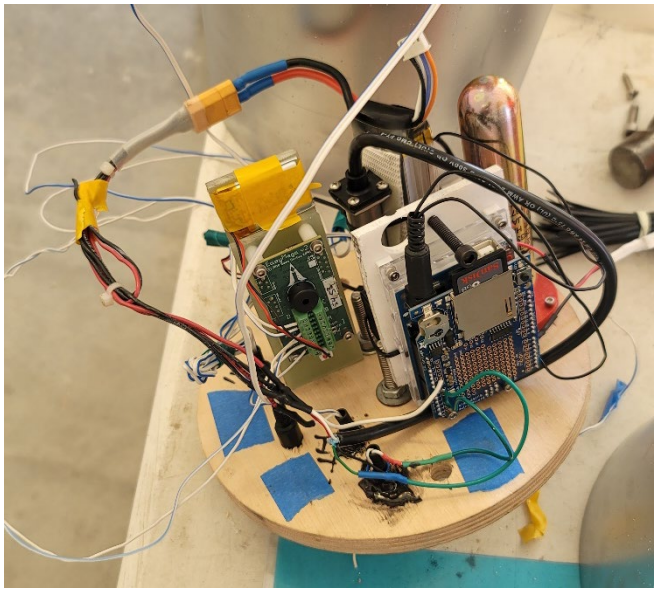

Figure 80. Sustainer avionics bay side view

3. Flight Data and Results

Although the stage separation and ignition appeared to function appropriately from the ground, the ground receiver lost contact with the Kate-1 telemetry system at a distance of 2.57 km (1.6 mi). Ground observers lost visual contact with the sustainer following sustainer motor burnout, and no parachute was able to be discerned, preventing recovery of the sustainer section. The loss in connection was thought to be due to the Kate-1 telemetry system not being properly configured to "launch mode."

Because of this, no quantitative data was collected on the performance of the aft nozzle enclosure cap. The only information available was anecdotal evidence from ground observations that suggested the four shear pin variant of the nozzle cap may have functioned as intended. The ignition of the rocket second stage was observed to occur very close to the two-second delay from booster burnout that was programmed into the EasyMega that controlled stage separation and sustainer ignition. The extra post-ignition delay that was observed in the onboard video captured during the previous launch was not present in this case. Furthermore, the ignition sound heard by observers on the ground was a loud, crisp "bang" that suggested there may have been an improvement in the motor thrust

time response over the previous launch. These observations, of course, require confirmation through further testing. Figures 81 and 82 show stills from video captured from the ground.

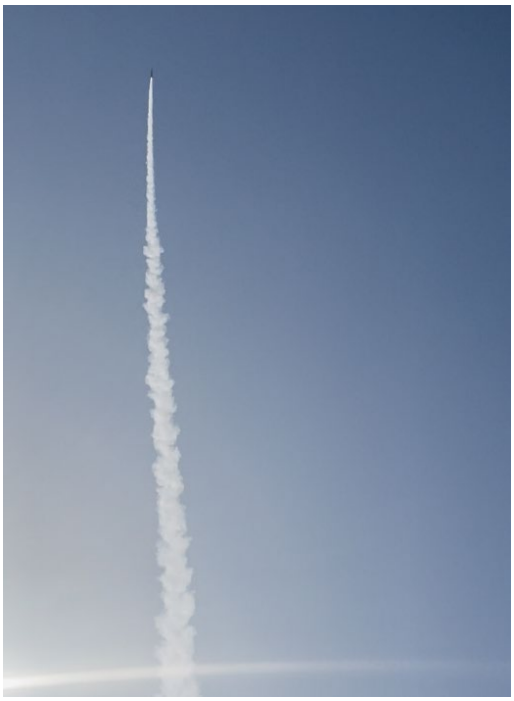

Figure 81. First stage boost phase T+2 seconds

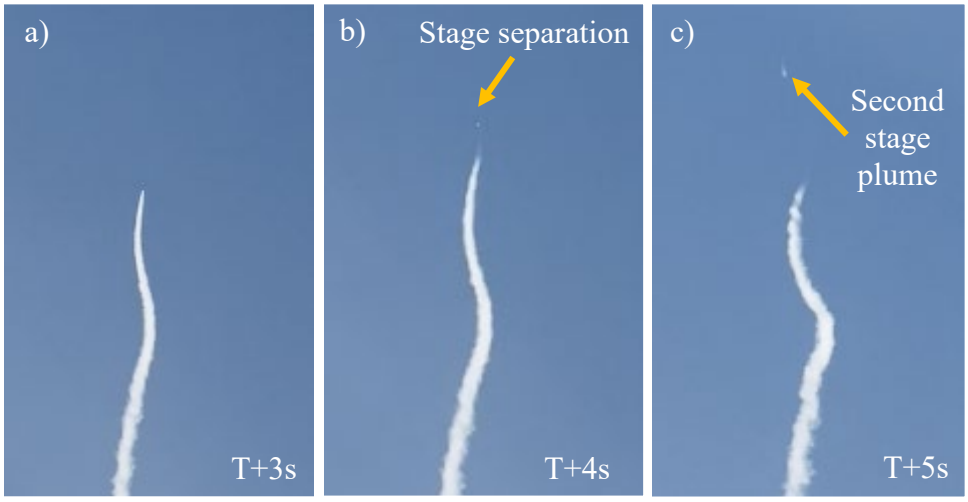

Figure 82. a) Booster burnout, b) stage separation, c) sustainer ignition

THIS PAGE INTENTIONALLY LEFT BLANK

VI. SUMMARY

Several modifications to COTS SRMs, including a head-end ignition system, a nozzle enclosure system, and a custom-designed blast tube, were investigated in support of the NPS RRPD-V. These modifications were designed to be manufactured at low cost and easily integrated into existing commercial motor hardware with minimal modifications to the hardware itself. To that end, 3D printing was heavily used as the preferred manufacturing technique. Alternative manufacturing methods were investigated and suggested for components that could not be 3D printed because of the pressure and thermal loads expected on the component.

The design of the head-end ignition system focused on three primary competing versions of a mechanism that held the ignition squib in place. For all versions, the squib was inserted through the forward motor hardware. The first two versions incorporated a perforated basket concept that directed hot jets that would contact and ignite the propellant. The third version was an open holder that did not restrict the size of the squib used or influence the direction of the expelled material. Ultimately, the open holder version was selected for flight tests because it allowed for a squib sizeable enough to reliably light the propellant, as demonstrated during live-fire ground testing, without presenting a significant threat of nozzle throat clogging. Two two-stage rocket launches demonstrated the ability of the head-end ignition system to reliably ignite the second-stage motor and be controlled by the avionics equipment onboard the rocket. The basket approach may still be viable but would require custom loading squib material into the basket to maximize the space available.

The nozzle enclosure system was designed to environmentally seal the motor chamber and propellant for long-term storage. During launch, the enclosure caused chamber pressure to build to a specified point before yielding and being expelled from the aft end of the rocket. This was intended to improve the transient ignition process of the motor by preventing the escape of exhaust prior to the ignition of the full burn area of the propellant, resulting in a more rapid increase in chamber pressure. Two sealing methods were tested—a plug that created a seal on the internal surface of the diverging section of

the nozzle and a cap that sealed around the external diameter of the nozzle. The main difference between these methods was the ability of the former to manipulate the pressure face area and, therefore, more precisely control the blowout chamber pressure. The benefit of the external seal method was reduced complexity of the enclosure geometry that led to a more reliable seal and a more modular "one-size-fits-many" system. Control of the blowout chamber pressure beyond the precision of adjusting the number of shear pins used to secure the cap to the retainer was deemed unnecessary to attain the desired results. The sustainer section of the rocket, which housed the pressure monitoring system, was lost during the second flight test and was not recovered. Anecdotal evidence observed by personnel at the launch suggested this enclosure method had the intended effect. More testing, however, is needed to draw firmer conclusions.

The final design effort proposed a design for a blast tube, which will favorably shift the SRM CG and allow for the simultaneous use of a larger diameter SRM and aft fin control servos. The design was intended to be seamlessly integrated into COTS hardware by replacing the commercial nozzle. The internal geometry of the tube was based on industry standards for COTS rocket nozzles, and the length could be extended or shortened based on the requirements of the GNC system of the RRPD-V. Finally, a potentially cost effective method of manufacture was proposed based on NASA practices, which involved wrapping layers of carbonized phenolic tape around a mandrel machined to the desired geometry.

VII. FUTURE WORK

A. HEAD-END IGNITION SYSTEM

Although the open version of the squib holder was selected for live-fire and flight tests for this study, the perforated basket version may still hold promise. Using a basket squib holder that is small enough to negate the risk of a nozzle clog would require the Rocket Lab to custom pour its own ignition squibs rather than use commercial pre-made squibs. This can be done with commercially available material but will require further testing. Benefits of using the custom-poured basket include higher repeatability in the energy of the squib ignition due to the more precise control of the amount of squib material used in the custom pour and quicker and easier assembly of pre-poured baskets into the head-end hardware.

B. NOZZLE ENCLOSURE SYSTEM

Further live-fire tests are needed to determine the enhancement, if any, to the efficiency of the SRM from the inclusion of the nozzle enclosure design. Whether the follow-on tests are conducted on the ground or in flight, the health monitoring system developed as part of this study could be used to collect the desired data. Future experiments may also wish to study how aging affects the propellant by comparing characteristics, such as burn rate, of samples of propellant that have been stored sealed versus open to atmospheric conditions.

C. BLAST TUBE

The blast tube will require the most extensive amount of future work, to include testing of the viability of the recommended, as well as competing, methods of manufacturing. Structural tests should be conducted to ensure the selected manufacturing material can withstand expected chamber pressure and thermal loads. Computational fluid dynamics should also be leveraged to ensure adequate heat absorption such that the components surrounding the blast tube are insulated from the exhaust flow. The final

design will need to be closely tailored to the requirements of the GNC system in order to ensure optimal SRM CG shift and adequate space for aft fin control servos.

D. ROCKET VEHICLE

Improvements can be made to the avionics equipment to increase redundancy and minimize risk of loss of data or equipment. In addition to the Kate-1 telemetry system, the TeleMega altimeters can be fitted with an antenna that allows telemetry data to be transmitted to a ground station in real time. Correspondence with the TeleMega vendor also revealed that TeleMegas can be special ordered with additional signal input pins that could allow data from the health monitoring system to be transmitted to the ground station in real time.

APPENDIX. DATA LOGGER ARDUINO CODE

```
/*
  SD card datalogger

  This example shows how to log data from three analog sensors
  to an SD card using the SD library.

  The circuit:
   analog sensors on analog ins 0, 1, and 2
   SD card attached to SPI bus as follows:
 ** MOSI - pin 11
 ** MISO - pin 12
 ** CLK - pin 13
 ** CS - pin 4 (for MKRZero SD: SDCARD_SS_PIN)

  created  24 Nov 2010
  modified 9 Apr 2012
  by Tom Igoe

  This example code is in the public domain.

*/

#include <SPI.h>
#include <SD.h>

const int chipSelect = 10;

char fileName[] = "LOGGER00.txt";
File dataFile;

void setup() {
  // Open serial communications and wait for port to open:
  Serial.begin(9600);
  while (!Serial) {
    ; // wait for serial port to connect. Needed for native USB port only
  }

  Serial.print("Initializing SD card...");

  // see if the card is present and can be initialized:
  if (!SD.begin(chipSelect)) {
    Serial.println("Card failed, or not present");
```

```
    // don't do anything more:
    while (1);
  }
  Serial.println("card initialized.");

  // create a new file
  for (uint8_t i = 0; i<100; i++){
    fileName[6] = i/10 + '0';
    fileName[7] = i%10 + '0';
    if (! SD.exists(fileName)){
      // only open a new file if it doesn't exist
      Serial.println("Creating file: ");
      Serial.println(fileName);
      break;
    }
  }
}

void loop() {
  // make a string for assembling the data to log:
  String dataString = "";

  // read three sensors and append to the string:
  for (int analogPin = 0; analogPin < 3; analogPin++) {
    int sensor = analogRead(analogPin);
    dataString += String(sensor);
    if (analogPin < 2) {
      dataString += ",";
    }
  }
  dataString += ",";
  dataString += String(millis());

  // open the file. note that only one file can be open at a time,
  // so you have to close this one before opening another.
  dataFile = SD.open(fileName, FILE_WRITE);

  // if the file is available, write to it:
  if (dataFile) {
    dataFile.println(dataString);
    dataFile.close();
    // print to the serial port too:
    Serial.println(dataString);
  }
  // if the file isn't open, pop up an error:
```

```
  else {
    Serial.println("error opening datalog.txt");
  }
}
```

THIS PAGE INTENTIONALLY LEFT BLANK

LIST OF REFERENCES

[1] Pledger, T., 2021, "The Role of Drones in Future Terrorist Attacks," AUSA [Online]. Available: https://www.ausa.org/publications/role-drones-future-terrorist-attacks

[2] Guitton, M. J., "Fighting the Locusts: Implementing Military Countermeasures Against Drones and Drone Swarms," *Scandinavian Journal of Military Studies*, Vol. 4, No. 1, p. 26-36, 2021, doi: 10.31374/sjms.53.

[3] "Rockets Galore; Cheap Smart Weapons," *The Economist (London)*, vol. 404, no. 8804, p. 85–, 2012.

[4] Busta, M., "Design and Development of an Adaptable Flight Demonstration Vehicle and Modular Guidance and Control," Master's Thesis, Mechanical and Aerospace Engineering Department, Naval Postgraduate School, Monterey, CA, 2019.

[5] Lobo, K., "Submunition Design for a Low-Cost Small UAS Counter-Swarm Missile," Master's Thesis, Mechanical and Aerospace Engineering Department, Naval Postgraduate School, Monterey, CA, 2018.

[6] Decker, K., "System Design and Integration of a Rapid Response Payload Delivery Vehicle Using Commercial Off-The-Shelf Components," Master's Thesis, Mechanical and Aerospace Engineering Department, Naval Postgraduate School, Monterey, CA, 2021.

[7] Thyberg, R., "Design and Testing of a Multi-Unit Payload Delivery and Tracking System for Guided Munitions to Combat UAV Swarm Threats," Master's Thesis, Mechanical and Aerospace Engineering Department, Naval Postgraduate School, Monterey, CA, 2019.

[8] Brophy, C., "ME4704 Missile Design Problem/Motivation," Mechanical and Aerospace Engineering Department, Naval Postgraduate School, Monterey, CA, 2021.

[9] Benson, T., "Rocket Stability," NASA Glenn Research Center, May 2021. https://www.grc.nasa.gov/www/k-12/rocket/rktstab.html

[10] H. Shekhar, "Prediction and Comparison of Shelf Life of Solid Rocket Propellants Using Arrhenius and Berthelot Equations," Propellants, explosives, pyrotechnics, vol. 36, no. 4, pp. 356–359, 2011, doi: 10.1002/prep.200900104.

[11] Cesaroni Technology, Pro75 6819M1540-P Motor Data, May 2009. http://www.pro38.com/products/pro75/motor/MotorData.php?prodid=6819M1540-P

[12] Arnold, C., Ong, W. X., Patrick, G., Stuffle, N., and Fick, A. "ME4704: Tactical missile Design High Altitude Communications Relay," Naval Postgraduate School, Monterey, CA, 2021.

[13] Ultimaker, Ultimaker PC Material Properties, Utrecht, Netherlands, retrieved 17 Mar. 2022. https://ultimaker.com/materials/pc

[14] Ultimaker, Ultimaker Tough PLA Material Properties, Utrecht, Netherlands, retrieved 17 Mar. 2022. https://ultimaker.com/materials/tough-pla

[15] Saraswat, V. K., Woodley Clive, and Reddy G. Satheesh, "Effect of Burn Rate Exponent Variation on Ballistic Performance of Gas Generator with High Burn Rate Propellant," in Ballistics 2019 - 31st International Symposium on Ballistics, Volume 1 & 2, DEStech Publications, 2019, pp. 1–2.

[16] Zipay, J., Clarence T. Modlin, and Curtis E. Larsen, "The Ultimate Factor of Safety for Aircraft and Spacecraft – Its History, Applications and Misconceptions," in *57th AIAA/ASCE/AHS/ASC Structures, Structural Dynamics, and Materials Conference*, doi: 10.2514/6.2016-1715.

[17] Hall, N., "Converging-Diverging Nozzle," *Nozzle Design*, NASA Glenn Research Center, May 2021. https://www.grc.nasa.gov/www/K-12/airplane/nozzled.html

[18] RocketMaterials.org, Sheer Pins, Rocket Materials, Scranton, PA, Aug. 2004. https://web.archive.org/web/20131026023457/http://www.rocketmaterials.org/datastore/cord/Shear_Pins/index.php

[19] Cesaroni Technology, Pro150, Ontario, Canada, retrieved 02 May 2022. http://www.pro38.com/products/pro150/pro150.php

[20] Marshal Space Flight Center, *Application of Ablative Composites to Nozzles for Reusable Solid Rocket Motors*, NASA Lesson Number 672, Feb. 1999.

[21] Cesaroni Technology, Pro98 9994M3400-P Motor Data, Ontario, Canada, Nov 2009. http://www.pro38.com/products/pro98/motor/MotorData.php?prodid=9994M3400-P

[22] Altus Metrum, *TeleMega*, Altus Metrum, Colorado Springs, CO, Sep. 2021.

[23] PerfectFlite, *StratoLoggerCF Altimeter*, PerfectFlite, Andover, NH, 2017.

[24] Altus Metrum, *EasyMega*, Altus Metrum, Colorado Springs, CO, Dec. 2021.

[25] Multitronix, *Kate-1 TelemetryPro Transmitter*, Multitronix, Boise, ID, retrieved 14 Apr. 2022.

[26] The Engineering ToolBox, *International Standard Atmosphere*, EngineeringToolBox.com, retrieved 16 Apr. 2022.

[27] Adafruit.com, "Overview," *Adafruit Data Logger Shield*, Adafruit, New York, NY, Apr. 2013.

THIS PAGE INTENTIONALLY LEFT BLANK

INITIAL DISTRIBUTION LIST

1. Defense Technical Information Center
   Ft. Belvoir, Virginia

2. Dudley Knox Library
   Naval Postgraduate School
   Monterey, California